

# A Liquid Scintillation Detector for Radioassay of Gadolinium-Loaded Liquid Scintillator for the LZ Outer Detector

S.J. Haselschwardt<sup>a,\*</sup>, S. Shaw<sup>a</sup>, H.N. Nelson<sup>a</sup>, M.S. Witherell<sup>a,b</sup>, M. Yeh<sup>c</sup>,  
K.T. Lesko<sup>b</sup>, A. Cole<sup>b</sup>, S. Kyré<sup>a</sup>, D.T. White<sup>a</sup>

<sup>a</sup>University of California (UC), Santa Barbara, Department of Physics, Broida Hall, Santa Barbara, CA 93106-9530, USA

<sup>b</sup>Lawrence Berkeley National Laboratory (LBNL), 1 Cyclotron Road, Berkeley, CA 94720-8099, USA

<sup>c</sup>Brookhaven National Laboratory (BNL) P.O. Box 5000, Upton, NY 11973-5000, USA

---

## Abstract

We report on the design and performance of the LUX-ZEPLIN (LZ) “Screener”, a small liquid scintillator detector consisting of  $\approx 23$  kg of LAB-based gadolinium-loaded liquid scintillator (GdLS) to be used in the LZ Outer Detector. The Outer Detector will be filled with 17.3 tonnes of GdLS and will surround the central liquid xenon time projection chamber of LZ. Its primary function will be to tag neutron events in the liquid xenon which could mimic a WIMP dark matter signal. To meet the deadtime requirements for the Outer Detector, the radioimpurity levels in the GdLS must be kept below  $\lesssim 0.07$  mBq/kg. This background level corresponds to a rate of  $\approx 50$  Hz above an energy threshold of 100 keV.

The Screener was operated in the ultra-low-background environment of the former LUX water shield in the Davis Laboratory at the Sanford Underground Research Facility for radioassay of the GdLS. Careful selection of detector materials and use of ultra-low-background PMTs allows the measurement of a variety of radioimpurities. The  $^{14}\text{C}/^{12}\text{C}$  ratio in the scintillator is measured to be  $(2.83 \pm 0.06(\text{stat.}) \pm 0.01(\text{sys.})) \times 10^{-17}$ . Use of pulse shape discrimination allows the concentration of isotopes throughout the  $^{238}\text{U}$ ,  $^{235}\text{U}$ , and  $^{232}\text{Th}$  chains to be measured by fitting the collected spectra from  $\alpha$  and  $\beta$  events. We find that equilibrium is broken in the  $^{238}\text{U}$  and  $^{232}\text{Th}$  chains and that a significant portion of the contamination in the GdLS results from decays in the  $^{227}\text{Ac}$  subchain of the  $^{235}\text{U}$  series.

Predictions for the singles rate in the Outer Detector are presented. The rate from radioimpurities above 100 keV in the GdLS is estimated to be  $97.9 \pm 6.4$  Hz, with  $65.5 \pm 1.9$  Hz resulting from  $\alpha$ -decays.

**Keywords:** Low-background, Gadolinium, Liquid scintillator

---

\*Corresponding author

Email address: [sjh@physics.ucsb.edu](mailto:sjh@physics.ucsb.edu) (S.J. Haselschwardt)

## 1. Introduction

Searches for rare events caused by a variety of existing or conjectured particle and nuclear physics phenomena often feature auxiliary detectors that surround the principal detector in order to identify and permit the rejection of undesired events that can cause a background to the sought-after signal. Examples include Compton-suppression in high-sensitivity  $\gamma$ -ray spectroscopy [1, 2] and in searches for neutrinoless double-beta decay ( $0\nu\beta\beta$ ) [3]; solar neutrino experiments [4, 5], and searches for dark matter [6, 7].

The LZ (LUX-ZEPLIN) experiment is a second generation direct dark matter detector [8, 9] under construction one mile underground (4300 meters water equivalent) in the Davis Laboratory of the Sanford Underground Research Facility (SURF) in Lead, South Dakota, USA [10]. LZ uses a 7 tonne central liquid xenon (LXe) target, arranged in a dual-phase time projection chamber (TPC), to seek evidence for nuclear recoils from a hypothesized galactic flux of Weakly Interacting Massive Particles (WIMPs). Two active detector elements surround the TPC: a layer of liquid xenon, the Xenon Skin (XS), optimized to detect  $\gamma$ 's, and the Outer Detector (OD), optimized to detect neutrons ( $n$ 's).

In this paper we describe studies undertaken at SURF with a small detector that we call the ‘‘Screener’’ to evaluate the liquid scintillator (LS) planned for use in the OD. A primary goal of these studies was to evaluate radioactive contamination levels of the LS, and determine whether it meets the requirements of the LZ experiment.

The LS used in large-mass experiments devoted to the detection of  $\nu$ 's is one of the most radiopure materials known [11, 12] and would easily satisfy the radiopurity requirements for LZ. The purpose of the LS detector in LZ is, however, to detect  $n$ 's, so the requirements are similar to those for the detectors in  $\bar{\nu}_e$  experiments, which are sensitive to the process  $\bar{\nu}_e + p \rightarrow e^+ + n$ . The addition of gadolinium (Gd) to LS (GdLS) enhances the efficiency for  $n$  detection [13] and has been used successfully in several  $\bar{\nu}_e$  experiments [14–17]. However, since these experiments benefit from the high flux of  $\bar{\nu}_e$  from nuclear reactors and have higher energy thresholds, the radiopurity of the GdLS was not a great concern. This study is designed to measure the radiopurity with the sensitivity needed for LZ. Other studies undertaken after this work was started [18, 19] have found that isotopes from the  $^{235}\text{U}$  chain can be present at a level far out of proportion to the usual relative abundance of  $^{235}\text{U}$  to  $^{238}\text{U}$ . That result had not been predicted, although in retrospect the enhanced level of  $^{231}\text{Pa}$  and/or  $^{227}\text{Ac}$  in Gd is understandable [20].

The GdLS mass of the detector described here is  $\approx 23$  kg, and runs lasted roughly 10 days. Backgrounds were suppressed by the following techniques: 1) photomultiplier tubes (PMTs) with extremely low radioactivity ( $\approx 1$  mBq/tube) designed for the LZ LXe TPC [21] were used to measure scintillation light; 2) the detector was operated inside the LUX shield of ultra-pure water [22]; and 3) pulse-shape discrimination (PSD) was used to detect  $\alpha$ 's with negligible background. These features enabled a single event sensitivity of  $\approx 10^{-4}$  mBq/kg for  $\alpha$ 's. Sensitivity for  $\beta$ 's and  $\gamma$ 's is generally worse, since PSD is not useful in removing backgrounds. The typical sensitivity needed to assess whether a particular isotope might interfere with the LZ experiment's physics goals is  $\approx 10^{-2}$  mBq/kg.

The power of the small detector described here enables it to perform a number of

measurements relevant for low-background LS. The detector is easily sensitive to  $^{14}\text{C}$  contamination at the  $^{14}\text{C}/^{12}\text{C}$  level of  $10^{-19}$ . Contamination with  $^{14}\text{C}$  is a background to the detection of pp neutrinos and other rare event physics [23, 24]. Additionally, the detector is capable of measuring deviations from secular equilibrium in the  $^{238}\text{U}$ ,  $^{235}\text{U}$ , and  $^{232}\text{Th}$  chains.

## 2. Requirements of LZ

Two active detector elements surround the LZ TPC: the XS, a 4 cm to 8 cm thick layer of liquid xenon, in the same cryostat as the TPC, and the OD, a  $\approx 60$  cm layer of LS doped with 0.1 % Gd by mass. A layer of ultra-pure water  $\approx 200$  cm thick surrounds the assembly, contained in a stainless steel tank, to attenuate  $n$ 's and  $\gamma$ 's emitted from the Davis Laboratory walls. A drawing of the entire LZ detector system is shown in Fig. 1.

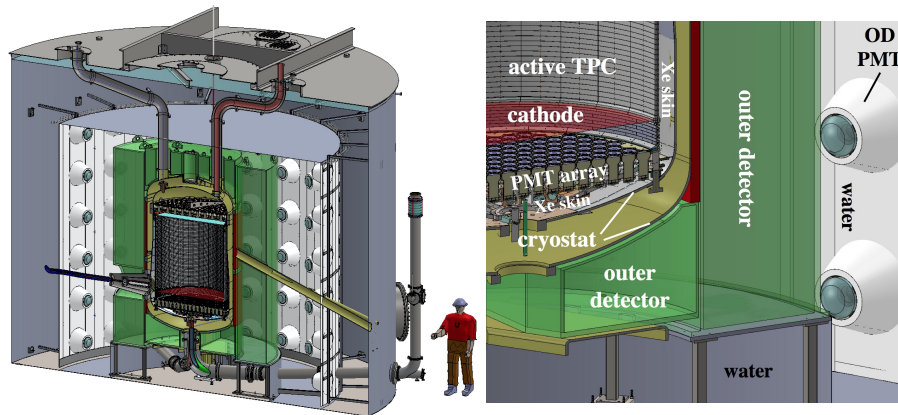


Figure 1: *Left:* A cutaway drawing of the LZ detector in the underground water tank from Ref. [9]. The OD acrylic tanks which hold the GdLS and surround the central TPC are shown in green. Light generated in the GdLS is collected in 120 PMTs which surround the tanks. A near-hermetic reflector system (white) aids in the OD light collection. *Right:* A zoomed view of the detector also taken from Ref. [9] showing details of the TPC internals, the XS region, and two OD PMTs. A full color version of this image is available online.

The signal sought in LZ is the recoil of a Xe nucleus in the TPC due to a collision with an impinging WIMP, accompanied by no energy depositions in the XS or the OD.

A variety of backgrounds to a WIMP signal arise from radioactive impurities in and near to the LXe TPC. An important class of backgrounds arise when a  $\gamma$  or a  $n$  is emitted due to a radioactive impurity in material on the perimeter of the LXe TPC, scatters once in the LXe TPC causing an energy deposit, and then exits. The XS has the principal power to veto  $\gamma$ 's, because of the small amount of material separating it from the LXe TPC, while the OD is designed to veto  $n$ 's. The LZ requirement is to achieve an efficiency for the detection of  $n$ 's which single-scatter in the LXe TPC of  $>95\%$ .

The main sources of  $n$ 's are the  $(\alpha, n)$  process and fission, both caused by uranium and thorium impurities in material surrounding the TPC. Neutrons of kinetic energy

$\approx 1$  MeV or higher can cause Xe recoils in the same energy window as those expected from a WIMP signal. The interaction length of 1 MeV  $n$ 's in LXe is about 11 cm, allowing a  $n$  from the perimeter to enter the LXe TPC, scatter once, exit, and then penetrate to the OD. Collisions with hydrogen in the LS rapidly moderate the  $n$ 's kinetic energy to a near-thermal level of a fraction of an eV. The  $n$  then diffuses until captured on a nucleus. In a predominantly hydrogenous material such as LS, the mean time to  $n$ -capture on a proton is  $\approx 220 \mu\text{s}$ , resulting in the emission of a 2.2 MeV  $\gamma$  and a deuteron.

Loading of Gd in LS exploits two  $n$ -capture properties of Gd. First, the thermal  $n$ -capture cross section of natural Gd,  $4.3 \times 10^4$  b, is large, so addition of only 0.1 % Gd by mass reduces the mean time to  $n$ -capture to  $\approx 30 \mu\text{s}$  [15]. Reduction of the time to  $n$ -capture can reduce the rate of false vetoes caused by accidental activity. The LZ goal of a probability of false veto  $< 5\%$  sets the maximum levels of radioactive impurities in and around the OD. Second,  $n$ -capture on Gd is followed by a cascade of several  $\gamma$ 's which release a total energy of  $\approx 8$  MeV. The probability of missing all of the several  $\gamma$ 's in this cascade is substantially lower than missing the single 2.2 MeV  $\gamma$  from capture on hydrogen.

The acrylic vessels which hold the GdLS influence the OD performance. Engineering and logistical considerations dictate that the tanks be built in segments at the vendor on the surface and then transported down to the Davis Laboratory. Four main side vessels surround the LXe cryostat in quadrants that together form a cylinder 375 cm tall; six small tanks cover the top and bottom of the cryostat. The radial GdLS thickness of 60 cm cannot be made thinner due to manufacturing concerns; consideration of  $n$  detection efficiency alone would permit thinner GdLS. The GdLS mass in the LZ OD is 17.3 tonnes.

The 2.5 cm thickness of the inner side acrylic tank wall, facing the LXe cryostat, is required for structural integrity. Simulations indicate that 5 % to 10 % of  $n$ 's emitted from the LXe TPC capture in the acrylic inner walls of the GdLS tanks, with a mean capture time characteristic of capture on protons:  $\approx 220 \mu\text{s}$ . To allow detection of these  $n$ 's, a time window for  $n$  detection of 500  $\mu\text{s}$  is set; the start of the time window will be a signal from the LXe TPC.

To achieve a probability of a false veto  $< 5\%$ , the singles rate in the OD system must be lower than 100 Hz above an energy threshold of 100 keV. Measurements and simulations predict a rate from  $\gamma$ 's emitted from the Davis Laboratory walls which penetrate the water shield, as well as from nearby LZ materials, of 50 Hz, allowing at most 50 Hz to arise from radioactive impurities in the GdLS.

Radioactive impurities in the GdLS consist of generally common isotopes and more unusual isotopes which enter with gadolinium. Common isotopes include  $^{14}\text{C}$ ,  $^{85}\text{Kr}$ ,  $^{40}\text{K}$ , and the isotopes in the  $^{238}\text{U}$  and  $^{232}\text{Th}$  chains. Unusual isotopes that enter with Gd include  $^{138}\text{La}$ ,  $^{147}\text{Sm}$ ,  $^{152}\text{Gd}$ ,  $^{176}\text{Lu}$ , and isotopes in the  $^{235}\text{U}$  chain. Approximately 40 isotopes produce energy deposits above a threshold of 100 keV, resulting in a specific activity for an average isotope that should not exceed 0.07 mBq/kg. Natural gadolinium contains 0.2 %  $^{152}\text{Gd}$  by weight, which contributes 1.6 mBq/kg in GdLS with 0.1 % gadolinium by mass. The signal from the 2.2 MeV  $\alpha$  from  $^{152}\text{Gd}$  is heavily quenched and emits light similar to that of a 100 keV  $\beta$  signal.

The abundance of other radioactive impurities can be influenced by chemical processing and purification of the components of GdLS. The specific activity levels reported by a variety of experiments which have used LS, as well as by experiments that use gadolinium, converted to the expectation in the GdLS described in this publication, are given in Tab. 1. Many of the specific activities exceed 0.07 mBq/kg.

Table 1: Summary of specific activities in units of mBq/kg, converted to a kilogram of LZ GdLS. To meet the LZ OD specifications, an average specific activity  $\leq 0.07$  mBq/kg is needed.

Isotope	Large Detectors Highest	GADZOOKS! Gd [19]		Boiko Gd [25]	
		Lowest	Highest	Purified	Raw
$^{14}\text{C}$	5000 [24]				
$^{40}\text{K}$	6.3 [26]	$< 1.9 \times 10^{-3}$	$0.25 \pm 0.01$	$< 0.04$	$< 0.09$
$^{85}\text{Kr}$	$0.88 \pm 0.02$ [27]				
$^{238}\text{U}_l/^{210}\text{Po}$	$0.20 \pm 0.05$ [15]				
$^{238}\text{U}_l/^{210}\text{Bi}$	$0.07 \pm 0.01$ [27]				
$^{238}\text{U}_l/^{210}\text{Pb}$	$0.06 \pm 0.01$ [27]				
$^{232}\text{Th}_e$		$< 3.9 \times 10^{-4}$	$2.12 \pm 0.02$	$< 0.005$	$0.09 \pm 0.01$
$^{232}\text{Th}_l$	$\approx 8 \times 10^{-3}$ [15]	$(5.8 \pm 4.0) \times 10^{-4}$	$0.97 \pm 0.01$		
$^{238}\text{U}_e$		$< 0.013$	$1.9 \pm 0.1$	$< 0.8$	$< 1.3$
$^{238}\text{U}_m$	$\approx 4.5 \times 10^{-4}$ [15]	$< 3.8 \times 10^{-4}$	$0.143 \pm 0.004$	$< 0.01$	$< 0.009$
$^{235}\text{U}_e$		$< 7.7 \times 10^{-4}$	$< 0.22$	$< 0.01$	$0.11 \pm 0.01$
$^{235}\text{U}_l$	$\approx 0.01$ [15]	$< 1.0 \times 10^{-3}$	$4.7 \pm 0.1$	$2.2 \pm 0.1$	$1.6 \pm 0.1$
$^{138}\text{La}$		$< 2.9 \times 10^{-4}$	$1.32 \pm 0.03$	$0.030 \pm 0.003$	$0.014 \pm 0.002$
$^{176}\text{Lu}$		$(4.4 \pm 1.7) \times 10^{-4}$	$1.09 \pm 0.01$	$0.035 \pm 0.003$	$0.038 \pm 0.004$

The two uranium decay chains and the thorium decay chain each contribute  $\approx 10$  unstable isotopes. A useful starting point is to assume that the isotopes in these chains are in secular equilibrium, with all isotopes within one chain, from the head ( $^{238}\text{U}$ ,  $^{235}\text{U}$ , and  $^{232}\text{Th}$ , respectively) to a step prior to the stable final isotope ( $^{206}\text{Pb}$ ,  $^{207}\text{Pb}$ , and  $^{208}\text{Pb}$ , respectively) contributing a rate equal to all other isotopes within the respective chain. Violations of secular equilibrium make the definition of subchains useful [28].

The subchains defined for  $^{238}\text{U}$  are shown in Fig. 2. Of the five isotopes in the early  $^{238}\text{U}_e$  subchain, three are long-lived, and are chemically similar, while the other two re-equilibrate rapidly after chemical processing. The six isotopes in the middle  $^{238}\text{U}_m$  subchain equilibrate rapidly with the chemically distinct  $^{226}\text{Ra}$  after processing. Emanation of  $^{222}\text{Rn}$  from surfaces contributes to  $^{238}\text{U}_m$ . The level of  $^{238}\text{U}_m$  is often measured in LS by the distinct  $\beta$ - $\alpha$  pulse pair from  $^{214}\text{Bi}$  and  $^{214}\text{Po}$ . Of the three radioactive isotopes in the late  $^{238}\text{U}_l$  subchain, the  $\beta$  from  $^{210}\text{Pb}$  has an energy below the OD threshold of 100 keV. Surfaces contain  $^{210}\text{Pb}$  deposited by environmental  $^{222}\text{Rn}$  and frequently contribute  $^{210}\text{Bi}$  and  $^{210}\text{Po}$  at rates higher than the other  $^{238}\text{U}$  subchains.

The subchains defined for  $^{235}\text{U}$  are shown in Fig. 3. The early  $^{235}\text{U}_e$  subchain contains two isotopes: the long-lived head of the chain,  $^{235}\text{U}$ , and the short-lived  $^{231}\text{Th}$ , which rapidly comes to equilibrium with  $^{235}\text{U}$  after chemical processing. The nine isotopes in the late  $^{235}\text{U}_l$  subchain start with the long-lived  $^{231}\text{Pa}$ , which is chemically distinct from uranium and not necessarily suppressed by chemical processes that sup-

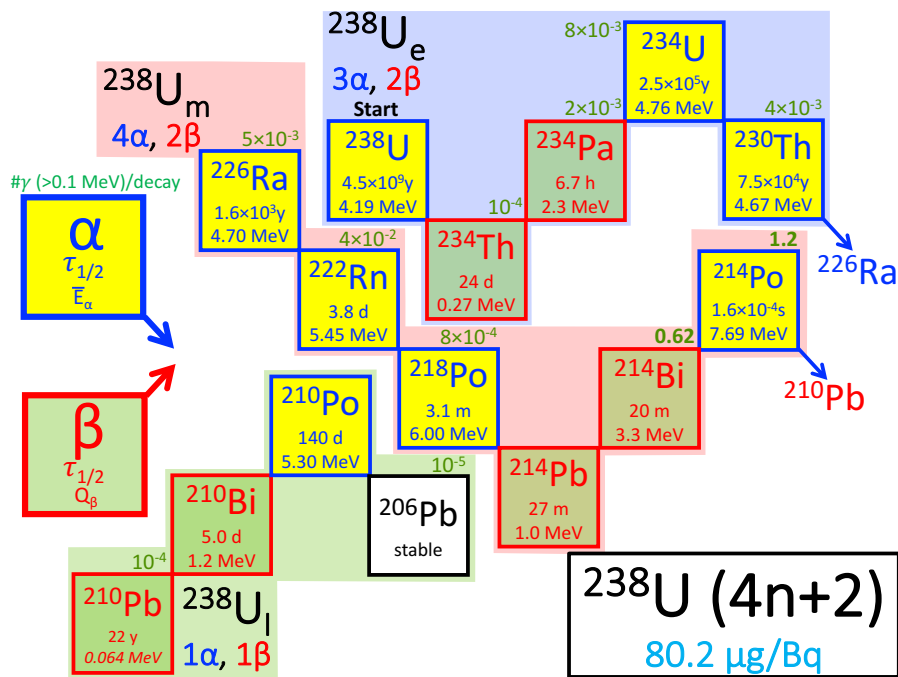


Figure 2: Definition of subchains for  $^{238}\text{U}$ . The 14 principal radioactive isotopes in the  $^{238}\text{U}$  decay chain are each shown in a box, with the half-life and energy released into  $\alpha$ 's and into  $\beta$ 's. The branching ratio into clear ( $>100$  keV)  $\gamma$ 's is shown in bold above the daughter, while for weak  $\gamma$  emitters, the largest branching ratio is shown. The one isotope with an energy release below the OD threshold,  $^{210}\text{Pb}$ , is not included in OD rate analyses or in the count of  $\beta$  decays shown. A full color version of this image is available online.

press uranium. While  $^{227}\text{Ac}$  is long-lived enough to re-establish equilibrium quickly after chemical processing, its chemistry may be similar enough to that of protactinium to stay in equilibrium following chemical processing. Both protactinium and actinium are chemically similar to gadolinium. The  $\beta$  from  $^{227}\text{Ac}$  has an energy below the OD threshold of 100 keV. The other seven isotopes in  $^{235}\text{U}_l$  rapidly re-equilibrate after chemical processing. The level of  $^{235}\text{U}_l$  can be measured in LS by the distinct  $\alpha$ - $\alpha$  pulse pair from  $^{219}\text{Rn}$  and  $^{215}\text{Po}$ .

The subchains defined for  $^{232}\text{Th}$  are shown in Fig. 4. Of the three isotopes in the early  $^{232}\text{Th}_e$  subchain, only the head isotope is long-lived, while the other two re-equilibrate rapidly after chemical processing. The  $\beta$  from  $^{228}\text{Ra}$  has an energy below the OD threshold of 100 keV. There are eight distinct radioactive isotopes in the late  $^{232}\text{Th}_l$  subchain, but weighting by the branching ratios of  $^{212}\text{Bi}$  reduces the count to seven. The isotopes in  $^{232}\text{Th}_l$  may rapidly re-equilibrate with  $^{228}\text{Th}$  after chemical processing, and are influenced by emanation of  $^{220}\text{Rn}$  from surfaces. The level of  $^{232}\text{Th}_l$  is often measured in LS by the distinct  $\beta$ - $\alpha$  pulse pair from  $^{212}\text{Bi}$  and  $^{212}\text{Po}$ .

The isotope with the highest specific activity in Tab. 1 is  $^{14}\text{C}$ . Use of under-

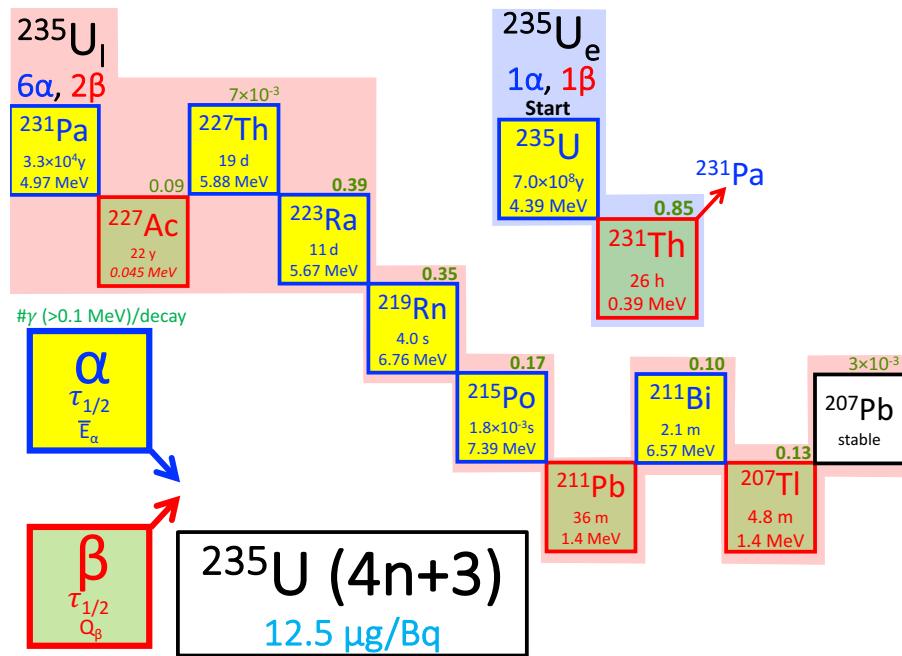


Figure 3: Definition of subchains for  $^{235}\text{U}$ . The 11 principal radioactive isotopes in the  $^{235}\text{U}$  decay chain are each shown in a box, with the half-life and energy released into  $\alpha$ 's and into  $\beta$ 's. The branching ratio into clear ( $>100$  keV)  $\gamma$ 's is shown in bold above the daughter, while for weak  $\gamma$  emitters, the largest branching ratio is shown. The one isotope with an energy release below the OD threshold,  $^{227}\text{Ac}$ , is not included in OD rate analyses or in the count of  $\beta$  decays shown. A full color version of this image is available online.

ground hydrocarbon sources for the LS chemicals results in  $^{14}\text{C}$  specific activities near 1 mBq/kg, while use of biogenic hydrocarbon sources caused the higher value in the table. The  $^{14}\text{C}$   $\beta$ -decay spectrum endpoint is 156.5 keV, with 8% of single pulses exceeding 100 keV. An increase of energy threshold can suppress single pulses from  $^{14}\text{C}$ , but multiple pulses from pileup of  $^{14}\text{C}$  decays during the planned LZ time window of 500  $\mu\text{s}$  can still be troublesome. The surveying technique of accelerator mass spectrometry has a sensitivity to  $^{14}\text{C}/^{12}\text{C}$  of  $10^{-15}$ , corresponding to a specific activity of 100 mBq/kg, which is not sufficient for the LZ OD. The desire to measure  $^{14}\text{C}/^{12}\text{C}$  with the required sensitivity is one of the principal motivations for building the Screener.

Isotopes in the  $^{235}\text{U}$  chain have been detected in gadolinium for GADZOOKS! [18] and also in GdLS at the level of 0.01 mBq/kg [15]. In Tab. 1, the specific activity per kg LZ GdLS is extrapolated from various samples studied in Ref. [19]. The lowest and highest values in Ref. [19] arise from variation among the samples obtained from different suppliers. Tab. 1 also shows the specific activities in LZ GdLS from the gadolinium evaluated in Ref. [25], both before and after purification. The highest  $^{235}\text{U}$

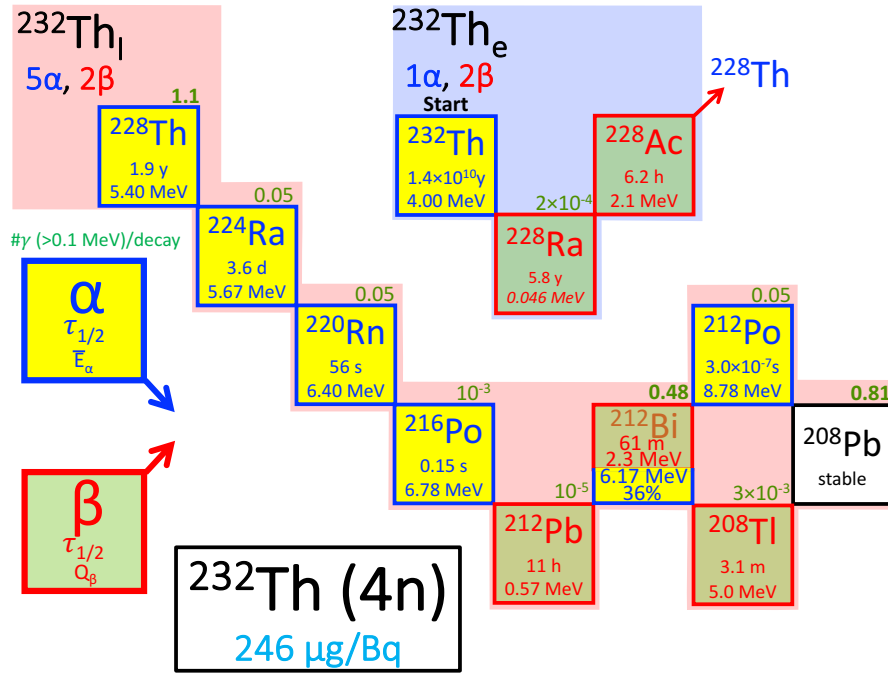


Figure 4: Definition of subchains for  $^{232}\text{Th}$ . The 11 principal radioactive isotopes in the  $^{232}\text{Th}$  decay chain are each shown in a box, with the half-life and energy released into  $\alpha$ 's and into  $\beta$ 's. The branching ratio into clear ( $>100$  keV)  $\gamma$ 's is shown in bold above the daughter, while for weak  $\gamma$  emitters, the largest branching ratio is shown. The one isotope with an energy release below the OD threshold,  $^{228}\text{Ra}$ , is not included in OD rate analyses or in the count of  $\beta$  decays shown. A full color version of this image is available online.

levels from both Gd studies exceed the specification for LZ GdLS.

Two radioactive isotopes are not included in Tab. 1. The first is  $^{152}\text{Gd}$ , which is unavoidable when using natural gadolinium and has  $\approx 60\%$  probability of exceeding a light output equivalent to a 100 keV  $\beta$  pulse. A rate in the OD of  $\approx 17$  Hz is expected from  $^{152}\text{Gd}$ .  $^{147}\text{Sm}$  emits an  $\alpha$  of energy 2.3 MeV, which will have a  $\approx 70\%$  chance of exceeding the light output of a 100 keV  $\beta$  pulse. The Screener is able to detect both of these  $\alpha$  emitters.

### 3. The Screener Detector System

#### 3.1. Physical Detector

Detector materials were chosen to minimize radioactivity near the LS volume, and all materials were screened by high-purity germanium (HPGe)  $\gamma$ -counting [29]. Plastic rather than metal components were favored to suppress radioimpurities.

The detector is comprised of a clear UV-transparent acrylic tube of inner diameter 29.2 cm and wall thickness 0.64 cm segmented along its length into three chambers, fabricated by Reynolds Polymer Technology, Inc. [30]. The partitions between cham-



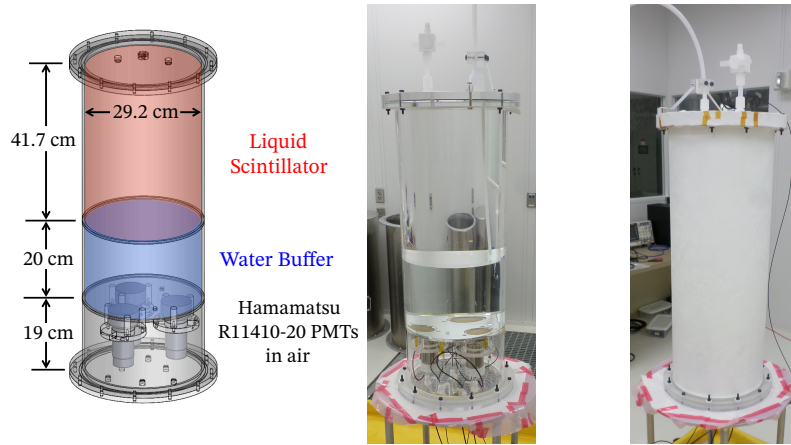


Figure 5: *Left*: Diagram of the detector vessel. *Middle*: The detector in the Davis Laboratory cleanroom with PMTs mounted, water and LS chambers filled. *Right*: The detector wrapped with Tyvek reflector before deployment. A full color version of this image is available online.

bers are 0.64 cm thick, and the chamber lids are 1.3 cm thick. The top chamber is 41.7 cm long and has a capacity of 28 L, so it can hold up to 24 kg of LS. The middle chamber is 20 cm long and is filled with 14.3 kg of distilled, deionized water that shields the LS from  $\gamma$ -rays generated in the PMTs. The bottom chamber is 19 cm long, filled with air, and holds the three low-background PMTs. The PMTs face the LS and are coupled to the acrylic wall between their chamber and the water volume using optical grease. The chambers on each end of the vessel are sealed by tightening 12 brass bolts and compressing an O-ring between the vessel flange and the chamber lid. The assembly is wrapped in 262  $\mu\text{m}$ -thick 1085D Tyvek [31, 32], which has a reflectivity  $\gtrsim 95\%$  over the range of GdLS light emission of 350 nm to 550 nm [33–35]. A diagram and two photographs of the detector are shown in Fig. 5.

The three PMTs are 7.6 cm Hamamatsu R11410-20, which have radioimpurity levels  $\approx 1$  mBq/PMT for the U/Th chain and  $(12 \pm 2)$  mBq/PMT for  $^{40}\text{K}$  [36]. The R11410-20 has a quantum efficiency of  $\approx 35\%$  at a wavelength of 420 nm, the peak of GdLS emission, and resolves single photoelectrons (phe) [21].

Two fill ports on the LS chamber lid allow for filling and venting of the chamber. A flexible line of concentric PTFE tubing is left on one of the ports during deployment. The inner tubing is converted to a rigid PTFE tube that extends into the bulk of the LS volume allowing nitrogen gas carrying  $^{220}\text{Rn}$  to be bubbled through the scintillator for calibration.

The detector was deployed in the former LUX water tank [22] just after the LUX detector was removed. The water shields from  $\gamma$ 's emitted from uranium, thorium, and potassium in the Davis Laboratory walls. The water tank height is 591 cm, and its radius is 381 cm. An inverted steel pyramid under the water tank of maximum thickness 30.5 cm and diameter 500 cm provides additional shielding from the rock in the floor. The stainless steel LUX detector stand was present in the water tank during the Screener deployment.

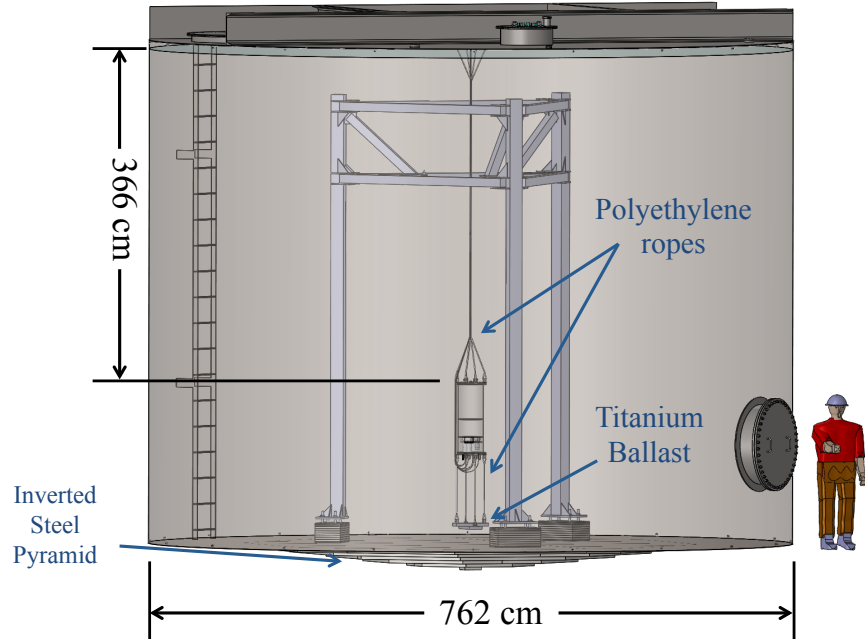


Figure 6: Deployment of the Screener in the water tank. The stand for the LUX detector is visible along with the inverted steel pyramid underneath the water tank floor. A full color version of this image is available online.

Polyethylene ropes suspended the detector assembly inside the water tank, as shown in Fig. 6. A 20 kg ballast of ultra-pure titanium [37] was suspended  $\approx 80$  cm from the bottom of the vessel to counteract the vessel buoyant force and to provide stability.

The vertical position in the water tank was chosen to minimize the rate from external  $\gamma$ 's originating from the LUX detector stand and from the Davis Laboratory walls. The  $\gamma$ 's from  $^{238}\text{U}$ ,  $^{232}\text{Th}$ ,  $^{40}\text{K}$ , and  $^{60}\text{Co}$  decays were described with a GEANT4-based [38] simulation package. At this location, there was 160 cm (366 cm) between the bottom (top) of the detector scintillator volume and the bottom (top) of the water volume. The estimated stand and wall contribution to the Screener rate is  $(0.57 \pm 0.03)$  mHz above an energy deposit threshold of 100 keV [39].

The resistivity and dissolved oxygen in the water was monitored during runs. An earlier measurement of radon in the nitrogen used to purge the water tank found a concentration of  $(0.054 \pm 0.026)$  Bq/m<sup>3</sup> while the dissolved oxygen was below the 1 ppb sensitivity of the oxygen monitor. Simulations predict a rate of  $(3.6 \pm 1.7)$  mHz above 100 keV from  $^{222}\text{Rn}$  decays in the water at this concentration.

The PMT signal and high voltage (HV) were provided via 13.7 m long RG174 and RG58 coaxial cables, respectively. Each cable was potted with epoxy into a watertight feedthrough in the PMT chamber lid, secured to the Screener vessel's top and bottom flanges and routed out of the water tank through a light-tight port. The cables

were then connected to the HV power supply and data acquisition system (DAQ) in a nearby electronics rack. Simulations indicate that the cables are the single largest source of background from construction materials, their contribution being 54 % of the total background rate. Screening of the cables had not been completed before deployment of the detector.

### 3.2. Electronics and Data Acquisition

The PMT signals went into charge sensitive amplifiers with high ( $40\times$ ) and low ( $4\times$ ) gain outputs for each input channel. Shaped and amplified waveforms were then digitized at 100 MHz by a SkuTek DDC-10 [40] digitizer and stored for off-line processing. Waveform digitization was triggered on the condition of coincident signals of greater than  $\approx 1.5$  phe in all three PMTs within a 50 ns time window. In this way, each PMT's  $\mathcal{O}$ (kHz) dark rate does not cause a significant number of triggers ( $< 1$  event in a 10 day run).

The digitized window for each trigger started  $2\ \mu\text{s}$  before the trigger and extended after the trigger by  $79.9\ \mu\text{s}$ . A subsequent trigger was re-enabled after writing the event to disk, which took on average 30 ms. The reconstruction of pulse pair rates when the second decaying nucleus has lifetime comparable to the digitization window or the re-enable time interval must account for deadtime.

The data were processed off-line by a pulse finding algorithm. The recorded waveforms were scanned for pulses and basic quantities such as the start and end times, area, and height were computed for each pulse found.

## 4. Liquid Scintillator

The LS solvent is linear alkylbenzene (LAB), chosen largely for its high flash point of  $130^\circ\text{C}$ , making LAB combustible, not flammable [41]. This simplifies safety mitigations required in underground laboratories. The other components of GdLS [42] are given in Tab. 2. The LAB is purchased from CEPESA [43], and is derived from underground sources, to minimize  $^{14}\text{C}$  content [44].

All components of the GdLS are purified [42, 45] with the exception of the bis-MSB (1,4-bis(2-methylstyryl)benzene) because of the extremely small quantity used in GdLS. The LAB solvent is purified by distillation, while the PPO (2,5-diphenyloxazole) is cleaned using recrystallization and water extraction. The Gd compound is purified by pH-controlled partial hydrolysis, during which Gd remains in solution while certain radioactive actinides such as uranium and thorium are precipitated out. Actinium itself, however, tends to remain in solution with Gd [45], resulting in an out-of-equilibrium level of  $^{227}\text{Ac}$ .

### 4.1. Optical Properties

Energy deposited in the GdLS causes excitations of LAB molecules. These excitations are transferred to PPO [46] resulting in the emission of fluorescent light, primarily below  $\lesssim 380\ \text{nm}$  [47]. The PPO fluorescent light is absorbed and re-emitted at longer wavelength [48] by bis-MSB (wavelength shifter) according to the spectrum shown at the top of Fig. 7. The emission spectrum peaks in the 410 nm to 425 nm range [49], well matched to the photocathode response of typical PMTs.

The GdLS light yield in response to a 662 keV  $\gamma$  is 53 % of anthracene [42]. A sim-

Table 2: Chemical components in 1 L of GdLS.

Acronym	Molecular Formula	Molecular Weight (g/mol)	Mass (g)
LAB	C <sub>17.14</sub> H <sub>28.28</sub>	234.4	853.55
PPO	C <sub>15</sub> H <sub>11</sub> NO	221.3	3.00
bis-MSB	C <sub>24</sub> H <sub>22</sub>	310.4	0.015
TMHA	C <sub>9</sub> H <sub>17</sub> O <sub>2</sub> <sup>-</sup>	157.2	2.58
Gd	Gd	157.3	0.86
GdLS	C <sub>17.072</sub> H <sub>28.128</sub> O <sub>0.0126</sub> N <sub>0.0037</sub> Gd <sub>0.0015</sub>	233.9	860.0

ilar electromagnetic energy deposited in anthracene needs  $(55 \pm 5)$  eV per transmitted 452 nm photon [50, 51], resulting in  $(10,000 \pm 1,000)$  photons/MeV in GdLS. The description of light yield for different specific energy depositions  $dE/dx$  will be described here by a generalized [52] Birk’s Law [53]:

$$\frac{dL}{dx} = Y \frac{dE/dx}{1 + kB(dE/dx) + C(dE/dx)^2} \quad (1)$$

Where  $Y$ , the light yield, as well as  $kB$  and  $C$  are parameters that are determined separately for electron recoils in response to  $\gamma$ ’s and for  $\alpha$ ’s [54] by the calibrations described in Sec. 6.

Optical photons traversing the GdLS may be absorbed by the liquid. The  $e$ -folding absorption length is shown at the bottom of Fig. 7. A long absorption length is desired for increased detection efficiency. The GdLS absorption length rises from  $\approx 1$  m at 410 nm to  $> 10$  m at 425 nm, resulting in little self-absorption of the emitted scintillation light.

#### 4.2. Screening of Gd Additives

A 0.307 kg sample of the same chelated Gd(TMHA)<sub>3</sub> compound dissolved in the Screener GdLS was counted for 18 d in a HPGe detector in the Berkeley Low Background Facility in the Black Hills Underground Campus [29]. Concentration causes the specific activity in mBq/kg as measured for the chelated compound to be 250 times higher than the specific activity for GdLS. Results from the HPGe exposure are reported in Tab. 3. The measured level of <sup>238</sup>U<sub>m</sub> may have been caused by radon contamination in the sample before the screening had started. The strong  $\gamma$ -line from <sup>235</sup>U (the head of the <sup>235</sup>U<sub>e</sub> subchain) was not detected. Due to the small sample mass and short counting period, the sensitivities achieved in this assay were too low for adequate characterization of the Gd impurities. However, the detection of <sup>176</sup>Lu was important for understanding the Screener data.

### 5. Data Collection and Calibrations

The Screener was shipped empty to the Davis Laboratory, where it was filled and commissioned in a cleanroom. When work was not being performed, the detector was

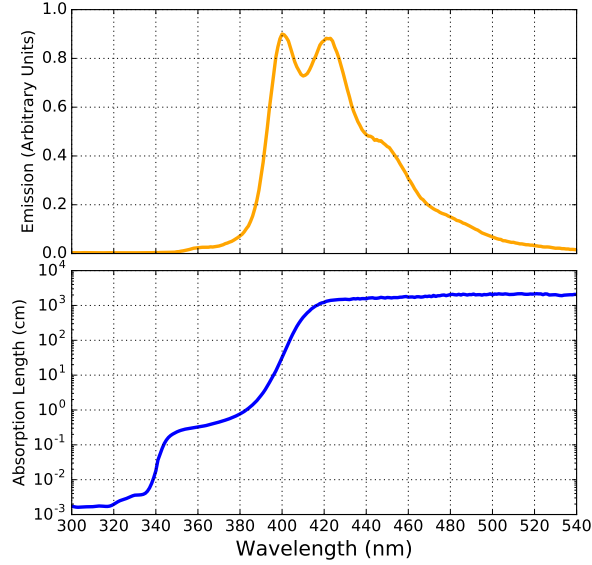


Figure 7: Wavelength dependence of key optical properties of the GdLS. *Top*: The emission spectrum of the GdLS scintillation light (in arbitrary units). *Bottom*: The absorption length of GdLS. A full color version of this image is available online.

Table 3: Results from HPGe counting of purified Gd(TMHA)<sub>3</sub> powder given in mBq/kg of Gd(TMHA)<sub>3</sub> and in mBq/kg of GdLS, loaded to 0.1% Gd by mass. To meet the LZ OD specifications, an average specific activity  $\leq 0.07$  mBq/kg of GdLS is needed. Limits are given at 68% CL and a systematic uncertainty of 10% is assumed on all values.

Isotope or Subchain	Measured	
	mBq/(kg Gd(TMHA) <sub>3</sub> )	mBq/(kg GdLS)
<sup>238</sup> U <sub>e</sub>	< 259	< 1.04
<sup>238</sup> U <sub>m</sub>	23 ± 5	0.092 ± 0.02
<sup>235</sup> U <sub>e</sub>	< 2.8	< 0.011
<sup>235</sup> U <sub>l</sub>	26 ± 10	0.10 ± 0.04
<sup>232</sup> Th <sub>e</sub>	< 6.7	< 0.027
<sup>232</sup> Th <sub>l</sub>	< 5.1	< 0.020
<sup>40</sup> K	< 56	< 0.22
<sup>138</sup> La	< 1.4	< 0.0055
<sup>176</sup> Lu	75 ± 18	0.30 ± 0.07

kept in a dark box continuously purged with nitrogen gas in order to limit exposure to the  $\approx 300$  Bq/m<sup>3</sup> [55] radon level in the Davis Laboratory air.

After commissioning, the detector was rolled out of the cleanroom on a cart and lifted off its stand with an overhead hoist. The detector was then lowered into the water tank and suspended by polyethylene ropes from hooks on the water tank ceiling as shown in Fig. 6. Cables and other services, including a gas line, an optical fiber, and radioactive sources were fed through a port in the water tank top. A check for light

leaks around the water tank port was performed once the PMTs were biased.

Data were taken in two runs. “Run 1” data were taken between November 2016 and early January 2017, using  $23.7 \pm 0.1$  kg of GdLS. Data in “Run 2” were taken between mid-January 2017 and February 2017, using the same scintillator mixture, but without Gd loading. In Run 2 the LS mass was  $23.2 \pm 0.1$  kg.

### 5.1. PMT Calibrations

The response of the PMTs was monitored  $\sim$ weekly with two types of single photoelectron calibrations. Light from a 420 nm LED in the DAQ system was fed through an optical fiber through the water tank port to the Screener to provide dedicated single photoelectron samples. Sometimes these calibration runs indicated drift in the PMT or amplifier response, so single photoelectron pulses in the midst of data taking were identified offline and used to correct drift during running. The PMT bias voltages were sometimes adjusted to equalize the single photoelectron response and were typically 1,385 V, 1,282 V, and 1,377 V.

### 5.2. Radioactive Source Calibrations

Several radioactive  $\gamma$  sources were used to calibrate the Screener response *in-situ* to energy deposited by electron recoils. For these calibrations the Screener was hoisted up to the water tank top, the sources were attached, and the assembly was lowered back into the tank.  $^{137}\text{Cs}$  and  $^{228}\text{Th}$   $\gamma$ -ray disk sources, in a tungsten collimator with a 1.75 cm-diameter aperture, were deployed on top of the Screener, and provide the principal electron recoil calibrations.

The detector response to energy deposits from  $\alpha$ 's,  $\beta$ 's, and  $\gamma$ 's was calibrated with a thoron ( $^{220}\text{Rn}$ ) source and its decay products (Fig. 4). The thoron source consisted of nitrogen gas flowed through a  $^{228}\text{Th}$  source; the gas was then bubbled into the the Screener scintillator volume. The signals from the thoron source have a distinct time dependence which we exploit: while nitrogen gas is flowing, a merged peak from the  $\alpha$ -decays of  $^{220}\text{Rn}$  and  $^{216}\text{Po}$  appear due to their relatively short half-lives (55 s and 0.14 s, respectively). These peaks promptly disappear once nitrogen flow is stopped. The population of daughter  $^{212}\text{Pb}$  atoms then feeds the rest of the chain according to its 10.6 h half-life. After roughly four days the thoron decay products had decayed to a level below that of the background rate.

Two thoron calibrations were performed in Run 1: the first after initial deployment of the detector in the water tank and the second prior to its removal. In Run 2, a single thoron calibration was performed prior to detector removal.

## 6. Detector Response Model

A detailed model of the detector geometry is implemented in the GEANT4 toolkit. The detector simulation models the deposition of energy in the detector materials and the generation, propagation, and detection of optical photons born in the LS.

### 6.1. Optical Model

The optical model includes the wavelength-dependent emission and absorption properties of the LS discussed in Sec. 4.1. The acrylic absorption length and the indices of refraction for GdLS and acrylic are also included [56].

The model also includes the re-emission probability of the GdLS shown in Fig. 8. This is the probability that an absorbed photon of a given energy is re-emitted according to the bis-MSB spectrum in Fig. 7. We found that agreement between  $^{228}\text{Th}$   $\gamma$  calibration data and the simulation could only be obtained by including this effect in the optical response of the GdLS. The 2.6 MeV  $\gamma$  from this source produces Compton electrons above the 180 keV Cherenkov threshold in GdLS. With the addition of the re-emission process in the model, the far-UV Cherenkov photons that are more heavily absorbed in GdLS can be re-emitted at longer wavelengths and detected more efficiently.

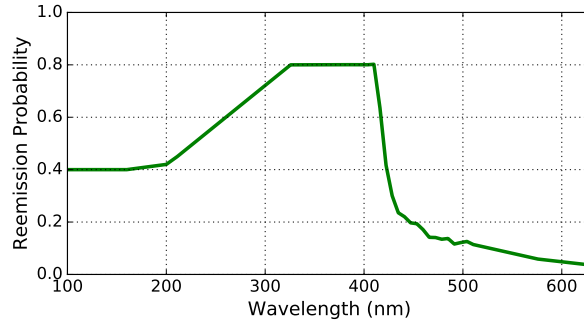


Figure 8: GdLS re-emission probability implemented in the optical model. A full color version of this image is available online.

The Tyvek surrounding the detector vessel is assumed to have the diffuse reflectivity dependence shown in Fig. 9. The shape of this dependence was measured in Ref. [34], while the overall scale was determined during surface commissioning of the detector where scintillator paddles above and below the vessel were used to tag Cherenkov events caused by muons traversing the acrylic vessel. The maximum reflectivity in the model is 98.1%. The reflectivity and the LS light yield parameters are somewhat degenerate in the task of modeling the total number of photons collected by the PMTs. An overestimate of the true Tyvek reflectivity will result in a corresponding underestimate of the scintillator light yield, but the total number of collected quanta will largely remain the same.

The generation of optical photons from energy deposits in the LS is implemented using the model in Eq. (1). The parameters  $Y$ ,  $kB$ , and  $C$  are determined by tuning the simulation to the calibration data collected in each run.

## 6.2. Calibration of Simulation Response

To calibrate the simulated detector response to energy deposits from electrons, different values of  $Y$  and  $kB$  are simulated and compared with  $^{137}\text{Cs}$  and  $^{228}\text{Th}$   $\gamma$  calibration data until good agreement via a  $\chi^2$  fit is obtained. The parameter  $C$  is set to zero for electron energy deposits. The  $kB$  parameter accounts for non-linearity in the scintillator response. Pulse area spectra for the best-fit parameters are shown with data in Fig. 10. The spectra of true energy deposits in the LS from these simulations show that the peaks in data are formed by the merging of a Compton edge and the corresponding

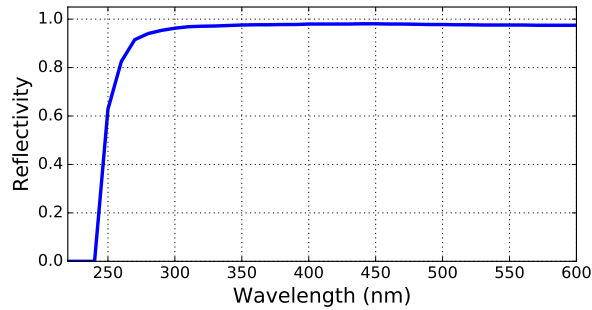


Figure 9: Wavelength dependence of the 1085D Tyvek reflectivity used in the detector optical model. A full color version of this image is available online.

photopeak.

The yield in phe/MeV in each run is determined by simulating energy deposits from electrons uniformly throughout the LS volume. The resulting distributions are skew Gaussian, a consequence of variation in light collection along the LS chamber vertical axis. The size of this variation is  $\approx 20\%$  across the full height. Simulations of uniform 1 MeV electrons in the LS give corresponding photoelectron yields of  $321 \pm 6$  phe/MeV in Run 1 and  $380 \pm 12$  phe/MeV in Run 2 using the mean values of the resulting skew Gaussian distributions. The error bars are obtained by varying  $Y$  and  $kB$  within their uncertainties and repeating the uniform electron simulations. These factors form the “approximate energy” scale used throughout this work; the non-linearity of the scintillator response with energy making it approximate. For the  $\alpha$  fit results shown in Sec. 7.5, an “approximate quenched energy” scale is shown, which reports  $\alpha$  energies as their electron-equivalent energy.

The detector response to  $\alpha$  events is similarly determined by simulating a set of  $\alpha$  energies for different values of  $kB$  and  $C$ . The mean number of collected phe in the simulation is compared to that from each peak in data with a  $\chi^2$ .

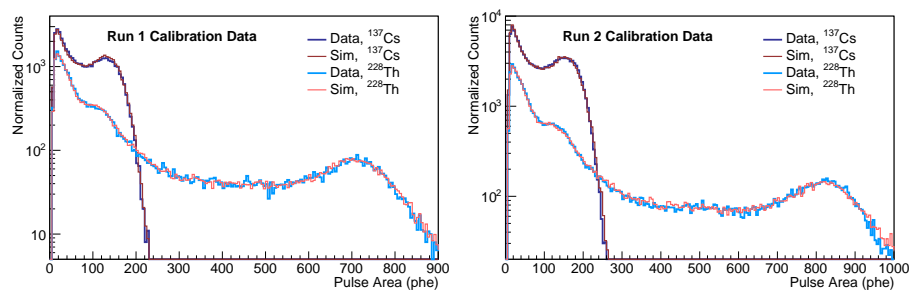


Figure 10: Pulse area spectra collected during calibrations with the  $^{137}\text{Cs}$  and  $^{228}\text{Th}$  sources. Overlaid are the simulated spectra obtained using the best fit  $Y$  and  $kB$  parameters. A full color version of this image is available online.



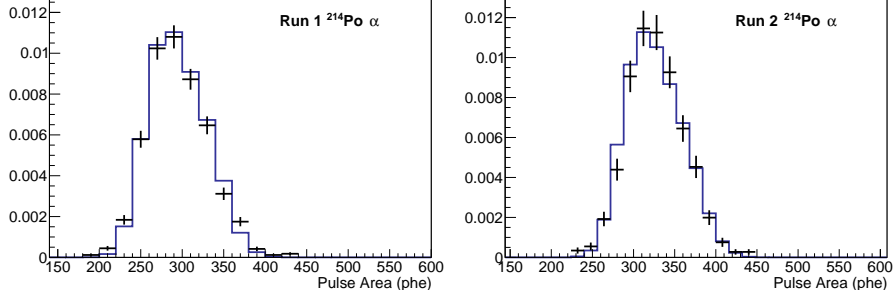


Figure 11: Pulse area spectra of  $^{214}\text{Po}$   $\alpha$ -decays in both runs obtained from BiPo coincidence cuts. The simulated spectra obtained using the best fit  $kB$  and  $C$  parameters are shown in blue. Both spectra have unit normalization. A full color version of this image is available online.

Early data from both runs provide an  $\alpha$  peak from dissolved  $^{222}\text{Rn}$ . The same data is analyzed for  $\beta$ - $\alpha$  coincidences from  $^{214}\text{Bi}$  to  $^{214}\text{Po}$  (“BiPo”) decays (see Section 7.2), allowing the construction of an  $\alpha$  peak from  $^{214}\text{Po}$ . This peak in data is shown in Fig. 11 along with the simulated response using the best fit  $kB$  and  $C$  parameters. Calibration data from the flow-through thoron source provides a merged peak from  $^{220}\text{Rn}$  and  $^{216}\text{Po}$  while the gas is flowing. Data collected after the flow has stopped provides peaks from  $^{212}\text{Bi}$  and  $^{212}\text{Po}$ , the former through its direct  $\alpha$ -decay (branching ratio 36 %) and the latter by identifying the prompt  $^{212}\text{Po}$   $\alpha$ 's following the  $\beta$ -decay of  $^{212}\text{Bi}$  (branching ratio 64 %). Finally, a merged, low energy peak from  $^{152}\text{Gd}/^{147}\text{Sm}$  decays is present in Run 1 data around  $\approx 30$  phe where GdLS was used (Fig. 14 left).

Comparisons of the same  $\alpha$  peak distributions during different thoron calibration periods show that the phe yield had changed during the calibration. It is likely that oxygen dissolved in the LS during the filling process was stripped by the active bubbling of nitrogen gas during the calibration. As a result, not all the available  $\alpha$  peaks are used for determining the  $kB$  and  $C$  parameters. In Run 1, the  $\alpha$  peaks from  $^{152}\text{Gd}/^{147}\text{Sm}$ ,  $^{220}\text{Rn}/^{216}\text{Po}$ ,  $^{212}\text{Bi}$ ,  $^{214}\text{Po}$ , and  $^{212}\text{Po}$  are used, while in Run 2 the peaks from  $^{222}\text{Rn}$ ,  $^{220}\text{Rn}/^{216}\text{Po}$ , and  $^{214}\text{Po}$  are used. Between calibrations, the phe yield is monitored using the position of the  $^{214}\text{Po}$  peak and found to be stable to within 12 % in Run 1 and 6 % in Run 2.

Table 4: Scintillator parameters deduced from tuning the GEANT4 detector simulation to  $\gamma$  and  $\alpha$  calibration data. Also shown are the associated  $\chi^2/\text{ndf}$  values for each of the fits.

Parameter	Run 1	Run 2
LS Light Yield, $Y$ (photons $\text{MeV}^{-1}$ )	$8783 \pm 57$	$10202 \pm 138$
$kB$ $\gamma$ 's (cm $\text{MeV}^{-1}$ )	$0.0299 \pm 0.0016$	$0.0288 \pm 0.0036$
$kB$ $\alpha$ 's (cm $\text{MeV}^{-1}$ )	$0.00512 \pm 0.00041$	$0.00744 \pm 0.00070$
$C$ $\alpha$ 's (cm <sup>2</sup> $\text{MeV}^{-2}$ )	$(2.43 \pm 0.43) \times 10^{-6}$	$(0.68 \pm 0.54) \times 10^{-6}$
$\gamma$ Fit $\chi_{\text{min}}^2/\text{ndf}$	55.7/46	56.7/46
$\alpha$ Fit $\chi_{\text{min}}^2/\text{ndf}$	3.3/3	1.5/1

Tab. 4 summarizes the best fit simulation parameters used in each run. The lower light yield (and hence the lower phe yield) observed in Run 1 is thought to be from exposure of the LS to air during the filling process. This is also believed to be the cause of the higher  $^{222}\text{Rn}$  rate at the beginning of that run.

The parameters  $kB$  and  $C$  describing  $\alpha$  quenching in the LS are different for the two runs. The difference arises from the inclusion of the low energy  $^{152}\text{Gd}/^{147}\text{Sm}$   $\alpha$  peak in the fit for Run 1. The values found here are generally consistent with those found in [57] where it is shown that a range of  $kB$  and  $C$  values can result in similar overall quenching. The differing values are therefore not a concern, as our focus is on the response to  $\alpha$ 's of energy 4 MeV to 9 MeV. This range contains  $\alpha$ -decays from the uranium and thorium decay chains.

### 6.3. Pulse Shape Discrimination

The timing profile of emitted photons in the LS is dependent on the particle type. Energy deposits from particles such as  $\alpha$ 's that produce large amounts of ionization along their track produce photons with a characteristically slower time profile compared to electrons [58]. This allows for PSD between  $\alpha$  and  $\gamma/\beta$  events.

We use a simple parameter, the ratio of the pulse height to area as the discrimination variable. For a fixed pulse area, the characteristically slower pulses from  $\alpha$ 's have a smaller height than those from electrons, providing separation between pulses from these particle types. In Fig. 12, pulses from the external  $^{228}\text{Th}$  source (magenta) are shown with data from the flow-through  $^{220}\text{Rn}$  source (cyan and blue) in the height-to-area ratio versus area plane. The separation between  $\alpha$  events and electron events is clear. As demonstrated in [58], better separation is possible when oxygen is removed from the LS, e.g. by thoroughly bubbling with nitrogen gas.

The  $\gamma$  and  $\alpha$  calibration data in each run are profiled by fitting a Gaussian function to the height-to-area ratio distributions found in slices of pulse area. The means and variances obtained from the fit in each slice are subsequently fit to a linear plus exponential model, thus defining  $\gamma/\beta$  and  $\alpha$  bands within the PSD space. The bands are shown also in Fig. 12.

Selections of  $\alpha$  and  $\gamma/\beta$  events are made using cuts on the PSD parameter. For  $\alpha$  events we take the PSD parameter to be  $3\sigma$  below the calibrated  $\gamma/\beta$  band mean. For  $\gamma$  and  $\beta$  events we define a cut on the PSD parameter which takes the linear plus exponential form used to describe the band shape. The cut is at least  $2\sigma$  above the calibrated  $\alpha$  band mean at all energies.

The leakage of  $\gamma/\beta$  events into the  $\alpha$ -selected data is negligible. In Run 1 the expected leakage is 26 events, while a total of 5823 events are accepted by the cut. In Run 2, the expected leakage is 9 events with 911 events passing the selection. The expected leakage of  $\alpha$  events into the  $\gamma/\beta$ -selected data is 65 and 16 events in Run 1 and Run 2, respectively, while the number of accepted  $\gamma/\beta$  events in the two runs are 7521 and 4702.

The cut efficiencies in Run 1 are shown in Fig. 13. The efficiencies for both cuts are calculated both directly from thoron and  $\gamma$  source calibration data and using the parameterization of the bands. In the region where calibration data is available, good agreement is found between the band parameterization and the data, justifying the use of the band model in regions where there is no calibration data.

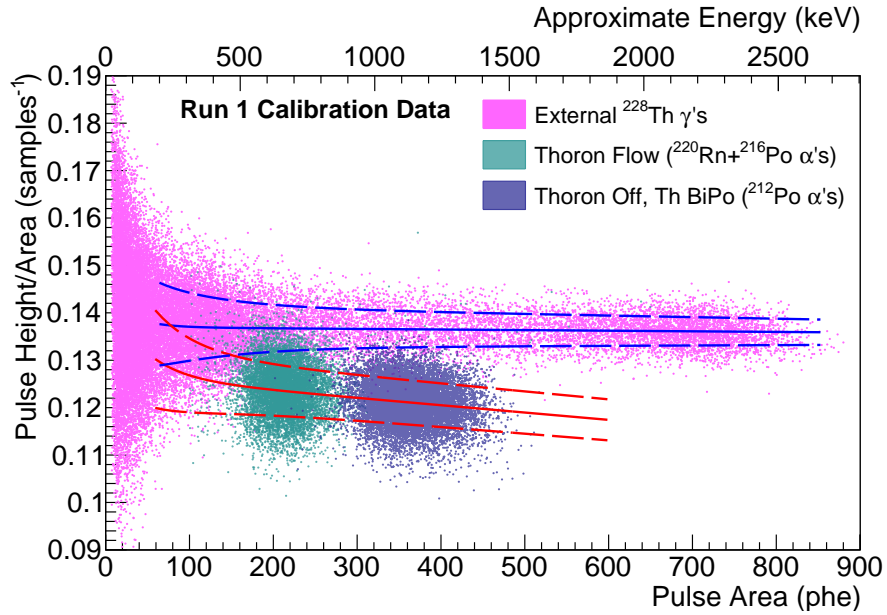


Figure 12: Calibration data with  $\alpha$ 's (cyan and blue) and  $\gamma$ 's (magenta) shown in PSD space. Overlaid are the fit  $\gamma$  (blue) and  $\alpha$  (red) band means (solid) and  $\pm 1\sigma$  (dashed) curves. A full color version of this image is available online.

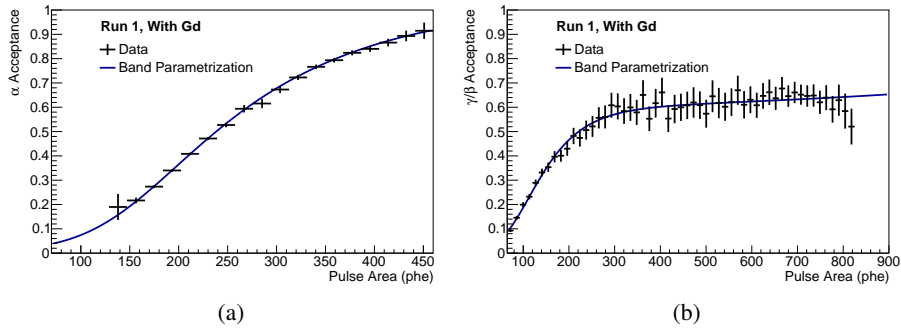


Figure 13: (a) Acceptance of  $\alpha$  events and (b)  $\gamma/\beta$  events as a function of pulse area computed using the Gaussian band parameterization of calibration data (blue) plotted with that computed using the data itself (black). Note that these are not fits. A full color version of this image is available online.

## 7. Measurement of Backgrounds in the LS

At the beginning of Run 1, the raw trigger rate was 2.3 Hz. Pulse area spectra from this early data show a clear peak from the  $\alpha$ -decay of  $^{222}\text{Rn}$  that decays in time consistent with the expected half-life of 3.8 d. This source of  $^{222}\text{Rn}$  is likely to have been dissolved in the scintillator while filling the vessel in the radon-rich underground environment. After approximately 21 days the trigger rate had plateaued to 0.3 Hz.

Similarly, spectra taken at the outset of Run 2 show a peak from  $^{222}\text{Rn}$ . The trigger rate was 0.32 Hz. After 14 days the plateaued trigger rate was 0.16 Hz. The smaller contamination from radon in Run 2 was a result of an improved LS filling procedure.

The plateaued rate at the end of each run arises from sources of radioactivity in the detector construction materials, the water tank/cavern environment, and the radioimpurities in the scintillator. We refer to data collected at the end of each run as “low-background” data.

The inclusive low-background data counting rates above 200 keV in the GdLS and LS runs are  $(78.6 \pm 0.4)$  mHz and  $(20.0 \pm 0.1)$  mHz, respectively. The collected pulse area distributions for each run are shown in Fig. 14. The livetime durations are 5.97 d for Run 1 and 11.83 d for Run 2.

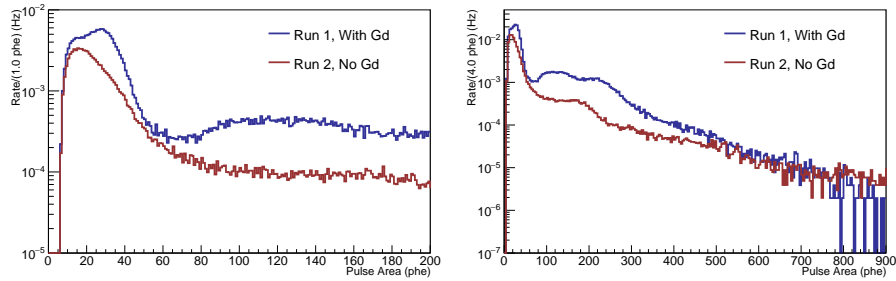


Figure 14: Run 1 and Run 2 low-background spectra shown in the low pulse area region (left) and over the full range of collected phe (right). The low energy peak at  $\approx 30$  phe from  $^{152}\text{Gd}/^{147}\text{Sm}$  decays is visible in the Run 1 data on the left. Note that Run 1 and Run 2 do not share the same energy scale (phe/MeV). A full color version of this image is available online.

The low-background data are divided into two primary regions:

1. Low pulse area region,  $\lesssim 250$  keV. The dominant source of rate in this region results from the  $\beta$ -decay of  $^{14}\text{C}$ . In Run 1, a peak results from the  $\alpha$ -decays of  $^{152}\text{Gd}$  and  $^{147}\text{Sm}$  that are quenched into this region.
2. High pulse area region,  $\gtrsim 250$  keV. Pulses in this region result from  $\gamma$  backgrounds external to the LS and from the decays of the internal radioimpurities dissolved in the LS. PSD is used in this region to select  $\alpha$  and  $\gamma/\beta$  events.

Specifically, the high pulse area region is defined by pulse areas  $>65$  phe, corresponding to  $>222$  keV, in Run 1 and  $>100$  phe, corresponding to  $>281$  keV, in Run 2. The inclusive count rates measured with these thresholds are  $(75.9 \pm 0.4)$  mHz and  $(16.0 \pm 0.1)$  mHz, respectively.

### 7.1. Measurement of $^{14}\text{C}$ Concentration

A measurement of the ultra-low  $^{14}\text{C}/^{12}\text{C}$  ratio in pseudocumene-based LS was performed by the Borexino collaboration and found to be at the  $10^{-18}$  level [44]. Here we follow nearly the same procedure to determine the  $^{14}\text{C}$  concentration in our LS by fitting the low pulse area region of Run 2 with the  $^{14}\text{C}$   $\beta$ -decay ( $Q = 156$  keV) shape.

The distribution of electron energies resulting from  $\beta$ -decay follows the form

$$N(W)dW = pW(W_0 - W)^2 F(Z, W)C(W)dW \quad (2)$$

where  $p$ ,  $W$ , and  $W_0$  are the electron momentum, energy, and endpoint energy in units of the electron mass, respectively. The Fermi function,  $F(Z, W)$ , corrects the kinematic shape by accounting for Coulomb interactions between the daughter nucleus and the electron. The distribution is further altered by a shape factor  $C(W)$ , which we take to have the form:

$$C(W) = 1 + aW. \quad (3)$$

As in [44], the tabulated values of the Fermi function in [59] were parameterized and used here.

The data in the low pulse area region is fit using the following convolution model:

$$R(W) = N_C \int N(W')G(W', W)dW' + N_{\text{bkg}}B(W) \quad (4)$$

Here,  $G(W', W)$  is a detector resolution function, which smears the true  $\beta$ -decay shape,  $N(W')$ . The  $^{14}\text{C}$  and background shapes are weighted by their corresponding number of events,  $N_C$  and  $N_{\text{bkg}}$ , respectively.

The detector resolution function,  $G(W', W)$ , is observed in data to be non-Gaussian. This is best seen in the distributions of various  $\alpha$  peaks, which are instead well-described by a skew-normal distribution with location, width, and skewness parameters  $\xi$ ,  $\omega$ , and  $\alpha$ , respectively:

$$f(x) = \frac{1}{\sqrt{2\pi}\xi} e^{-\frac{(x-\xi)^2}{2\omega^2}} \operatorname{erfc} \left[ \frac{-\alpha(x-\xi)}{\sqrt{2}\omega} \right] \quad (5)$$

This description of  $G(W', W)$  is accurately predicted by the simulation as a result of variations in light collection efficiency with position. The associated mean and variance of the skew-normal distribution are given by

$$\begin{aligned} \mu &= \xi + \omega\delta\sqrt{\frac{2}{\pi}}, \\ \sigma^2 &= \omega^2 \left( 1 - \frac{2}{\pi}\delta^2 \right), \end{aligned} \quad (6)$$

with

$$\delta = \frac{\alpha}{\sqrt{1 + \alpha^2}}.$$

Simulations of uniform energy deposits within the detector volume show that the detector resolution is well modeled by

$$\frac{\sigma}{\mu} = \sqrt{k_1^2 + \frac{k_2^2}{\mu}}. \quad (7)$$

At higher energies where  $\gamma$  calibration data is available, the first term dominates the resolution behavior. For fitting the low pulse area region, we fix  $k_1$  to have the value of 0.087 predicted by the Monte Carlo and allow  $k_2$  to float in the fit.

Extrapolation of the background simulations from Section 7.4 into the low pulse area region indicate that the background shape underlying the  $^{14}\text{C}$  spectrum is well described by a decaying exponential plus a linear term. The integral of this shape then determines the number of background events,  $N_{\text{bkg}}$ , which is fixed during the fit.

The fit is performed between 20 and 80 phe. The following parameters are allowed to float freely:

- The number of  $^{14}\text{C}$  events,  $N_C$
- The scale factor that converts energy deposited in the LS to the observed number of phe,  $Q/E$  (phe/MeV)
- The constant  $k_2$  in the detector resolution model, Eq. (7)
- The parameter  $a$  in the  $\beta$ -decay shape factor,  $C(W)$ .

From the fit number of  $^{14}\text{C}$  decays, the concentration  $^{14}\text{C}/^{12}\text{C}$  is calculated as

$$f(^{14}\text{C}/^{12}\text{C}) = \frac{A \tau M_{\text{LAB}}}{17.1 m_{\text{LS}} N_A} \quad (8)$$

where  $A$  is the fit  $^{14}\text{C}$  activity and  $\tau$  is the  $^{14}\text{C}$  mean lifetime (8,266.6 y).  $M_{\text{LAB}}$  is the molar mass of LAB (233.9 g/mol) and  $m_{\text{LS}}$  is the mass of LS in the detector during the run. The average number of carbon atoms in LAB is 17.1 and  $N_A$  is Avogadro's number. Eq. (8) returns the ratio  $^{14}\text{C}/^{12}\text{C}$  as an atom fraction, not a mass fraction<sup>1</sup>.

A good fit is obtained to the Run 2 data and shown in Fig. 15. A summary of the best fit values for the various parameters is given in Tab. 5. The  $^{14}\text{C}/^{12}\text{C}$  value is given with a statistical error bar from the fit and a systematic error resulting from the uncertainty on the LS mass in the detector. The statistical uncertainty is larger than expected from pure event counting because of correlations between the number of  $^{14}\text{C}$  decays, the energy scale, and energy resolution parameters. Precise knowledge of these parameters in the low-energy region from dedicated calibrations would improve the sensitivity of detectors similar to the Screener.

Our results are consistent with the  $^{14}\text{C}/^{12}\text{C}$  ratio of  $(3.3 \pm 0.5) \times 10^{-17}$  measured in LAB-based LS in Ref. [60], though our error is approximately a factor of  $8\times$  smaller. The level of contamination we measured here satisfies the requirements of the LZ OD. The expected  $^{14}\text{C}$  rate above 100 keV in the OD is  $(7.0 \pm 0.2)$  Hz.

---

<sup>1</sup>Both conventions are used in the literature, often without clear definition of units.

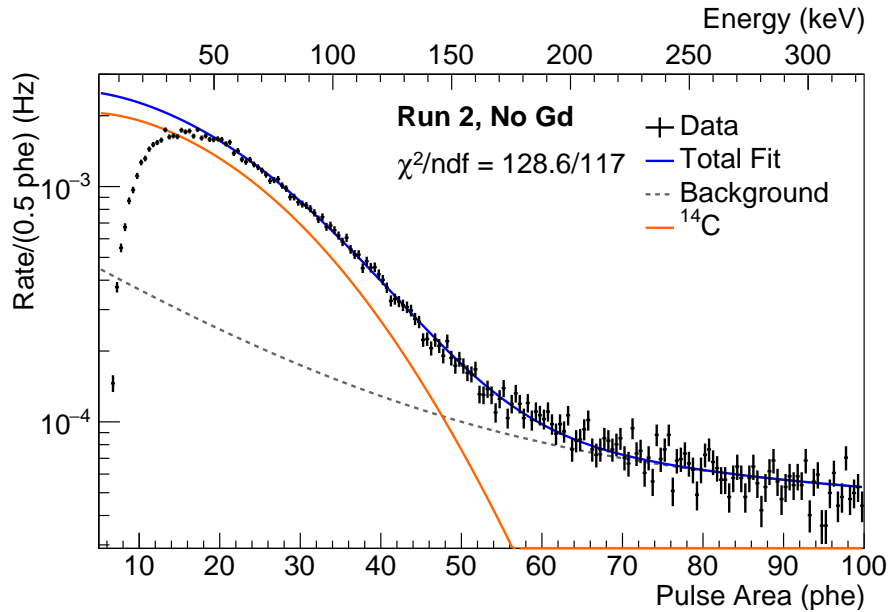


Figure 15: Run 2 low pulse area data shown with the best fit to the background plus  $^{14}\text{C}$   $\beta$  model. Shown at the top of the plot is the energy axis derived from the best-fit energy scale factor. A full color version of this image is available online.

## 7.2. $\beta$ - $\alpha$ and $\alpha$ - $\alpha$ Coincidence Rates

As mentioned in the introduction, the  $^{238}\text{U}_m$ ,  $^{235}\text{U}_1$ , and  $^{232}\text{Th}_1$  subchains are commonly measured by directly counting  $\beta$ - $\alpha$  or  $\alpha$ - $\alpha$  coincidences. Each of these subchains contains a short-lived polonium isotope which allows a coincidence tag with the previous decay in the series. The relevant polonium half-lives in these three subchains are  $164\ \mu\text{s}$  ( $^{214}\text{Po}$ ),  $1.78\ \text{ms}$  ( $^{215}\text{Po}$ ), and  $299\ \text{ns}$  ( $^{212}\text{Po}$ ), respectively.

Pulse pairs consistent with the expected  $\alpha$  and  $\beta$  energies are counted in two coincidence windows within the larger  $81.9\ \mu\text{s}$  event window:  $5\ \mu\text{s}$  to  $76\ \mu\text{s}$  for the  $^{238}\text{U}$  and  $^{235}\text{U}$  chains and  $0.4\ \mu\text{s}$  to  $4\ \mu\text{s}$  for the  $^{232}\text{Th}$  chain. The deadtime following each event prevents the use of larger windows for  $^{214}\text{Po}$  and  $^{215}\text{Po}$  decay. The PSD value of the first pulse in a coincident pair distinguishes the  $\beta$ - $\alpha$  events from the  $^{238}\text{U}$  chain and the  $\alpha$ - $\alpha$  events from the  $^{235}\text{U}$  chain. The accidental coincidence background is largest when selecting  $\beta$ - $\alpha$  events in the  $^{238}\text{U}$  chain and is calculated to be 0.08 events, making this measurement essentially background-free. Requiring that the second pulse ( $\alpha$  pulse) be consistent with the expected quenched alpha energy removes background from PMT afterpulses, as they have much smaller pulse areas [61].

The efficiency for selecting events with pulse pairs within each timing window is calculated analytically using the half-life of the polonium decay. The efficiency of cuts on pulse area (and therefore deposited energy) is assessed through simulation. The total efficiencies for the  $^{238}\text{U}$ ,  $^{235}\text{U}$ , and  $^{232}\text{Th}$  chain selections in Run 1 (Run 2) are 21.7% (21.9%), 2.7% (2.7%), and 32.1% (32.6%), respectively. The largest source

Table 5: Results of fitting data in the low pulse area region from 20-80 phe with the  $^{14}\text{C}$  + background model in Run 2.

Run 2: Livetime = 11.83 d; LS Mass = $(23.2 \pm 0.1)$ kg; Fit $\chi^2/\text{ndf} = 128.6/117$	
Parameter	Fit Result
Shape factor, $a$ ( $\text{MeV}^{-1}$ )	$-0.34 \pm 0.12$
Resolution Parameter, $k_2$ ( $\text{phe}^{1/2}$ )	$1.57 \pm 0.07$
Energy scale ( $\text{phe MeV}^{-1}$ )	$309 \pm 4$
$^{14}\text{C}$ Activity (mBq)	$110.7 \pm 2.4$
Concentration $^{14}\text{C}/^{12}\text{C}$ ( $\times 10^{-17}$ )	$2.83 \pm 0.06(\text{stat.}) \pm 0.01(\text{sys.})$

of inefficiency results from the choice of coincidence windows, a limitation imposed by the maximum event length of the DAQ. The dominant error on the double-pulse efficiency arises from the DAQ resolution in time, which is 10 ns, causing at most an error in efficiency of 0.9% for the  $^{232}\text{Th}$  chain selection and 0.01% for the  $^{238}\text{U}$  and  $^{235}\text{U}$  chain selections.

The subchain activities measured by coincidence counting in both runs are summarized in Tab. 6. The larger activities in the GdLS are consistent with the expectation that impurities enter through the Gd-loading process. In particular, it was demonstrated in Ref. [45] that the purification process for the Gd compound can efficiently remove thorium, but does not remove actinium. Similar difficulty in removing isotopes of protactinium from Gd compounds was observed in Ref. [25] due to its chemical similarity with rare-Earth metals. We therefore suppose that  $^{231}\text{Pa}$  and/or  $^{227}\text{Ac}$  introduced during Gd-loading serves as the source of the  $^{235}\text{U}_1$  subchain activity measured here. No events consistent with the  $^{235}\text{U}_1$  subchain sequence are observed in the unloaded LS data.

Table 6: Concentrations of various subchains calculated from the measured coincidence rates in each run.

Subchain	Run 1 (mBq/kg)	Run 2 (mBq/kg)
$^{238}\text{U}_m$	$0.019 \pm 0.003$	$0.023 \pm 0.002$
$^{235}\text{U}_1$	$0.18 \pm 0.02$	$< 0.0037$ (90% CL)
$^{232}\text{Th}_1$	$0.0071 \pm 0.0019$	$0.00082 \pm 0.00074$

### 7.3. Fit to $\alpha$ Events

All of the  $\alpha$  decays in the  $^{238}\text{U}$ ,  $^{235}\text{U}$ , and  $^{232}\text{Th}$  chains contribute to the event rate in the Screener and are distinguished from other sources by using the PSD selection discussed in Sec. 6.3. Fits to the pulse area spectra of selected  $\alpha$  events are performed to measure the isotope activities throughout these chains.

Probability density functions (PDFs) in pulse area for the primary  $\alpha$ -emitting isotopes in the  $^{238}\text{U}$ ,  $^{235}\text{U}$ , and  $^{232}\text{Th}$  chains are created by simulating 50k decays of each uniformly in the LS volume. The distributions of collected phe are then weighted by the measured phe-dependent acceptance (Fig. 13a) to obtain the expected shapes for each isotope.

Isotopes from the same subchains are summed to reduce the overall number of



fit parameters. This results in six isotope populations:  $^{238}\text{U}_e$ ,  $^{238}\text{U}_m$ ,  $^{210}\text{Po}$ ,  $^{235}\text{U}_1$ ,  $^{232}\text{Th}$ , and  $^{232}\text{Th}_1$ . The  $^{235}\text{U}_1$  PDF is not used in the Run 2 fit as no signature for this chain was found in Sec. 7.2. The coincidence rates measured in Sec. 7.2 constrain their associated subchain PDF normalizations during the fit. The remaining populations float freely.

The large stopping power of  $\alpha$ 's restricts their origin to the LS itself or the inside acrylic surface of the LS chamber. In the latter case, radon daughter plate-out results in  $^{210}\text{Po}$   $\alpha$ 's depositing their energy in the LS with minimal energy loss in the acrylic due to their  $\sim 100$  nm implantation depth. This is short compared to the typical range of these  $\alpha$ 's in acrylic which is  $\approx 30$   $\mu\text{m}$ .

An upper limit on the  $^{210}\text{Po}$  surface activity is known from counting a  $\sim$ year old sample of acrylic from the manufacturer of the Screener vessel. The sample had no protective coating during its exposure time. An XIA UltraLo-1800  $\alpha$  counter [62] measured a  $^{210}\text{Po}$  surface activity of  $(3.0 \pm 0.7)$  mBq/m<sup>2</sup> on this sample. The inside surface area of the Screener LS chamber is 0.52 m<sup>2</sup>, while only half the  $^{210}\text{Po}$   $\alpha$ 's interact in the LS. This gives the conservative upper limit of  $(0.8 \pm 0.2)$  mHz in the Screener. Given that the Screener is constructed of virgin acrylic and was kept in a nitrogen atmosphere whenever possible, the true surface activity is likely much smaller and so is ignored here.

#### 7.4. Fit to $\gamma/\beta$ Events

Complementary fits are performed to spectra of  $\gamma/\beta$  events selected using the cut described in Sec. 6.3. Subchain equilibrium suggests that activity measured through  $\alpha$ -decays should have a concomitant activity through  $\beta$ -decays. The populations included in these fits are summarized here.

Event distributions resulting from sources of radioactivity external to the LS are obtained by simulation of decays in the detector construction materials. The expected number of counts from external  $^{238}\text{U}$ ,  $^{232}\text{Th}$ , and  $^{40}\text{K}$  are then obtained by normalizing to the detector material radioassay results from HPGe counting. The contribution from  $^{222}\text{Rn}$  decays in the surrounding water is also included. The rate from  $^{60}\text{Co}$  in the detector materials was found to be negligible.

In the  $^{238}\text{U}$ ,  $^{235}\text{U}$ , and  $^{232}\text{Th}$  chains, there are six, four, and five primary isotopes that decay by  $\beta$  emission, respectively. Of these,  $^{234}\text{Th}$ ,  $^{210}\text{Pb}$ ,  $^{227}\text{Ac}$ ,  $^{231}\text{Th}$ , and  $^{228}\text{Ra}$  are excluded as their  $\beta$ -decay endpoints fall below the range of the fit. As was done in the  $\alpha$  fits, isotopes belonging to the  $^{238}\text{U}_m$ ,  $^{235}\text{U}_1$ , and  $^{232}\text{Th}_1$  subchains are summed and constrained by the coincidence rates measured in Sec. 7.2. The isotopes that remain are allowed to float free, namely:  $^{234}\text{Pa}$ ,  $^{210}\text{Bi}$ ,  $^{228}\text{Ac}$ .

The cosmic ray flux of protons and neutrons on the Earth's surface leads to the production of the isotope  $^7\text{Be}$  through reactions on  $^{12}\text{C}$  in the LS. The resulting electron capture decay of  $^7\text{Be}$  can enter as a source of background through its emission of a 478 keV  $\gamma$ -ray 10.4 % of the time. The 53 d half-life of  $^7\text{Be}$  means that the surface production rate and decay rate were very likely in equilibrium for both the loaded and unloaded LS used here. The expected rate of 478 keV  $\gamma$ -rays from  $^7\text{Be}$  in the pseudocumene-based LS used by Borexino was estimated in [63]. By scaling those results and accounting for time spent underground (about 48 d and 29 d in Run 1 and 2, re-

spectively), we might expect  $\approx 1$  mBq of  $\gamma$ -emitting  $^7\text{Be}$  decays in the low-background data from each run. An independent estimate performed using the ACTIVIA software package [64] predicts a rate about a factor of  $3\times$  higher (demonstrating the large uncertainty associated with the activation rates). A PDF for  $^7\text{Be}$  decay is included in the fits for both runs.

Another possible contaminant is  $^{85}\text{Kr}$ . Present at the level of  $\sim 1$  Bq/m<sup>3</sup> in atmospheric air,  $^{85}\text{Kr}$  decays primarily by emission of a 252 keV  $\beta$  with a half-life of 10.7 y. In 0.434 % of these decays, the daughter nucleus is left in a meta-stable state with half-life 1.01  $\mu\text{s}$ . The deexcitation of this state results in the emission of a 514 keV  $\gamma$  that can be tagged in coincidence with the  $\beta$ . A set of selection cuts similar to those in Sec. 7.2 were devised to search for these coincidences in each run with total cut efficiencies of 13.6 % and 11.7 % with errors of at most 0.5%. Two events pass these cuts in Run 1, while a single event passes in Run 2. The expected backgrounds from accidental coincidences are 0.035 and 0.003 events. The resulting concentrations fall within the intervals [0.07, 0.81] mBq/kg and [0.01, 0.36] mBq/kg at 90 % CL, respectively. These are consistent with estimates of the air exposure during filling, which make use of the initial rates of  $^{222}\text{Rn}$  in each run.  $^{85}\text{Kr}$  populations in each fit are constrained with these normalization intervals. In the much larger OD, preventing  $^{85}\text{Kr}$  contamination during LS filling will be crucial.

In summary, the following populations are included with constraint terms in the fit: external U, Th, K, water  $^{222}\text{Rn}$  decays,  $^{238}\text{U}_m$ ,  $^{235}\text{U}_1$  (Run 1 only),  $^{232}\text{Th}_1$ ,  $^{176}\text{Lu}$  (Run 1 only), and  $^{85}\text{Kr}$ . The following populations are included and allowed to float freely:  $^{234}\text{Pa}$ ,  $^{210}\text{Bi}$ ,  $^{228}\text{Ac}$ ,  $^7\text{Be}$ , and  $^{40}\text{K}$ .

### 7.5. Fit Results

Our strategy is to regard the  $\alpha$  fits as the most robust technique for measuring the scintillator impurities. This comes about as a result of two observations: first, the shapes resulting from  $\alpha$  events are more distinct than those from  $\gamma/\beta$  events, which tend to be relatively featureless and can overlap significantly. Second, the  $\gamma/\beta$  fits suffer from having the external activity of the detector components as a background and contain a larger number of fit parameters.

The results from all fits are summarized in Tab. 7, where isotopes are grouped according to their decay chain. Where subchain results are given, the specified activity represents the activity of each isotope within the subchain. In general, we find consistency between the  $\alpha$  fits and the  $\gamma/\beta$  fits within the various subchains where equilibrium is expected. Activity is measured in the early parts of both the  $^{238}\text{U}$  and  $^{232}\text{Th}$  chains different than that measured by  $\beta$ - $\alpha$  coincidences, demonstrating that secular equilibrium is broken. The elevated activity of the GdLS with respect to the unloaded LS sample is obvious. The inclusive Screener rates above 200 keV reconstructed from Tab. 7 are  $(89.5 \pm 7.3)$  mHz in Run 1 and  $(25.1 \pm 3.0)$  mHz in Run 2, which are generally consistent (within  $1.7\sigma$ ) with those measured in data.

The isotope concentrations measured in the Screener generally agree with those obtained by the HPGe assay in Tab. 3. The largest discrepancy between those results and the Screener results is in the  $^{232}\text{Th}_e$  subchain concentration. In the HPGe analysis this subchain is measured using  $\gamma$  lines following the decay of  $^{228}\text{Ac}$ . The sensitivity of the Screener to this  $\beta$ -emitting isotope is poor, however the Screener is able to detect

the  $\alpha$ -decays from  $^{232}\text{Th}$  at the head of the subchain directly. As the Screener and HPGe detectors measure different isotopes in the subchain, the discrepancy between the two may be explained by a breakage of subchain equilibrium at the long-lived  $^{228}\text{Ra}$  isotope which has a half-life of 5.8 y.

The  $\alpha$  fits are shown in Fig. 16. In the unloaded LS of Run 2, the prominent feature is from out-of-equilibrium  $^{210}\text{Po}$  decay. In the GdLS, the  $\alpha$  rate is mostly comprised of decays from the  $^{235}\text{U}_1$  subchain, resulting in a smaller error on its concentration than that obtained from  $\alpha$ - $\alpha$  coincidences.

The  $\gamma/\beta$  fits are shown in Fig. 17 and provide a useful cross-check for the  $\alpha$  results. In the Run 2  $\gamma/\beta$  fit the best-fit values for the external uranium, external potassium, and water  $^{222}\text{Rn}$  activities are in general agreement with their predicted values. The amount of external thorium found by the fit is roughly a factor of two lower than predicted, but well constrained by the highest pulse area data. As the external conditions in each run were the same, we use the best-fit value found in Run 2 to rescale the external thorium constraint for the GdLS fit in Run 1.

Table 7: Measured radioimpurity concentrations in both loaded and unloaded LS runs grouped by isotope type. Reported errors are statistical only and, where none are given, the one-sided upper limit at 90% CL is reported. A 0.4% systematic error resulting from the uncertainty on the LS mass in the detector also applies.

	Isotope	Gd-Loaded LS Activity (mBq/kg)	Unloaded LS Activity (mBq/kg)	Method
<b><math>^{238}\text{U}</math> Chain</b>	$^{238}\text{U}, ^{234}\text{U}$	$0.23 \pm 0.02$	-	$\alpha$ Fit
	$^{238}\text{U}, ^{234}\text{U}, ^{230}\text{Th}$	-	$0.0055 \pm 0.0052$	$\alpha$ Fit
	$^{234}\text{Pa}$	$0.33 \pm 0.04$	$< 0.065$	$\gamma/\beta$ Fit
	$^{238}\text{U}_m$ Subchain	$0.019 \pm 0.003$	$0.023 \pm 0.002$	BiPo
	$^{210}\text{Bi}$	$0.40 \pm 0.26$	$0.30 \pm 0.10$	$\gamma/\beta$ Fit
	$^{210}\text{Po}$	$0.16 \pm 0.02$	$0.099 \pm 0.009$	$\alpha$ Fit
<b><math>^{235}\text{U}</math> Chain</b>	$^{235}\text{U}_1$ Subchain	$0.185 \pm 0.006$	-	$\alpha$ Fit
<b><math>^{232}\text{Th}</math> Chain</b>	$^{232}\text{Th}$	$0.16 \pm 0.04$	$0.059 \pm 0.013$	$\alpha$ Fit
	$^{228}\text{Ac}$	$< 0.20$	$< 0.018$	$\gamma/\beta$ Fit
	$^{232}\text{Th}_1$ Subchain	$0.0071 \pm 0.0019$	$0.00082 \pm 0.00074$	BiPo
<b>Other</b>	$^{40}\text{K}$	$< 0.34$	$< 0.14$	$\gamma/\beta$ Fit
	$^7\text{Be}$	$< 2.69$	$1.67 \pm 0.51$	$\gamma/\beta$ Fit
	$^{85}\text{Kr}$	$< 0.31$	$0.069 \pm 0.067$	$\gamma/\beta$ Fit
	$^{176}\text{Lu}$	$0.25 \pm 0.07$	-	$\gamma/\beta$ Fit

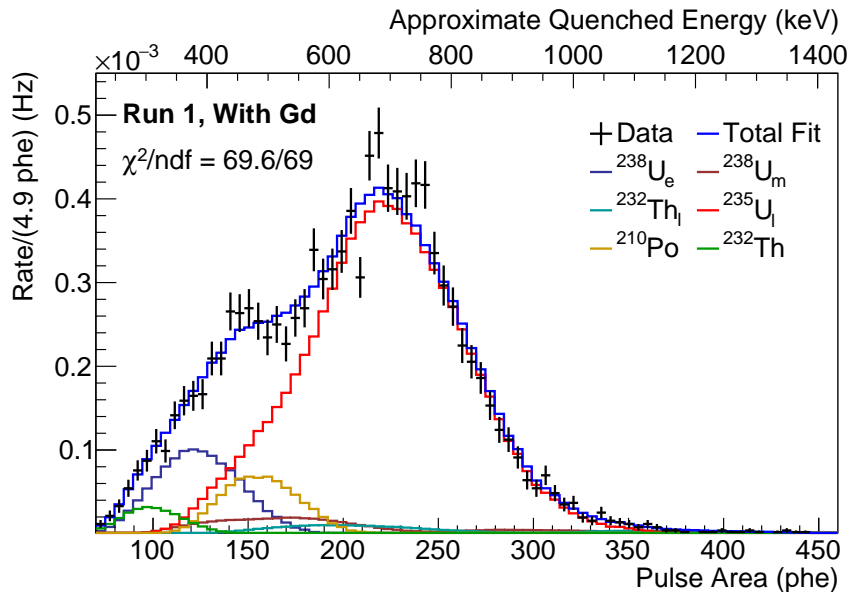
Our hypotheses regarding the locations of decay chain equilibrium breakage are motivated by the purification methods used to prepare the LS and GdLS discussed in Sec. 4. Both the water extraction and distillation techniques have demonstrated efficient removal of heavy elements, in particular, lead and radium [65, 66]. In comparison, the Gd compound's purification effectively removes thorium, but is not effective at removing actinium as previously discussed in Sec. 7.2. Our hypotheses are therefore the following: in the unloaded LS sample of Run 2 we expect that equilibrium is broken at the long-lived radium isotopes  $^{226}\text{Ra}$  ( $\alpha$  emitter,  $^{238}\text{U}$  chain) and  $^{228}\text{Ra}$  (soft  $\beta$  emitter,  $^{232}\text{Th}$  chain). In the GdLS, we expect that efficient thorium removal leads to breaks at the long-lived thorium isotopes  $^{230}\text{Th}$  ( $\alpha$  emitter,  $^{238}\text{U}$  chain) and  $^{228}\text{Th}$  ( $\alpha$

emitter,  $^{232}\text{Th}$  chain).

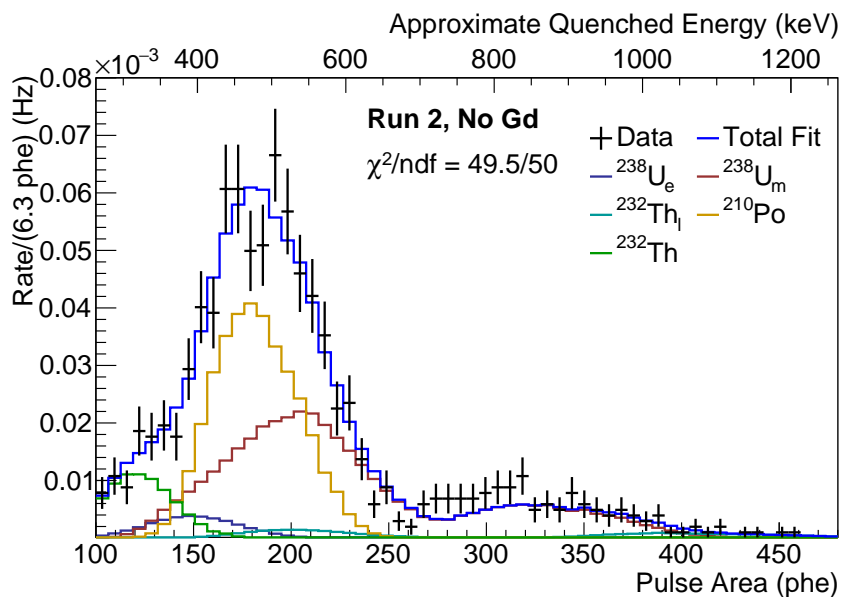
The most sensitive test for finding the location of equilibrium breakage is in the  $\alpha$  fits for each run. The  $\alpha$  emitters  $^{238}\text{U}$  through  $^{226}\text{Ra}$  in the  $^{238}\text{U}$  chain are successively removed from the BiPo-constrained  $^{238}\text{U}_m$  population and allowed to float freely, both independently from one another and as a summed  $^{238}\text{U}_e$  population. The fit  $\chi^2/\text{ndf}$  from each iteration is recorded in Tab. 8. Improvement in the Run 1 fit is observed with the removal of isotopes up to  $^{230}\text{Th}$ , after which the improvement is very small. A similar improvement is observed in Run 2, however, the case where no early  $^{238}\text{U}$  chain isotopes are excluded from the  $^{238}\text{U}_m$  population yields an acceptable  $\chi^2$  at 90% CL. This is reflected in Tab. 7 where the concentration of  $^{238}\text{U} + ^{234}\text{U}$  is consistent with the measured BiPo coincidence rate.

Table 8:  $\chi^2$  values obtained when various  $^{238}\text{U}$  early chain isotopes are allowed to float free, independent from the BiPo-constrained,  $^{238}\text{U}_m$  PDF ending with  $^{214}\text{Po}$ . Also given are the  $\chi^2$  values when those early chain isotopes are summed into a single, early chain PDF.

Early $^{238}\text{U}$ Chain Isotopes	Run 1 $\chi^2/\text{ndf}$		Run 2 $\chi^2/\text{ndf}$	
	Free	Summed	Free	Summed
None	147.4/70		63.2/51	
$^{238}\text{U}$	95.9/69	95.9/69	58.4/50	58.4/50
$^{238}\text{U}, ^{234}\text{U}$	68.1/68	69.6/69	50.4/49	50.4/50
$^{238}\text{U}, ^{234}\text{U}, ^{230}\text{Th}$	68.0/67	69.1/69	49.5/48	49.5/50
$^{238}\text{U}, ^{234}\text{U}, ^{230}\text{Th}, ^{226}\text{Ra}$	68.0/66	68.9/69	49.1/47	49.4/50

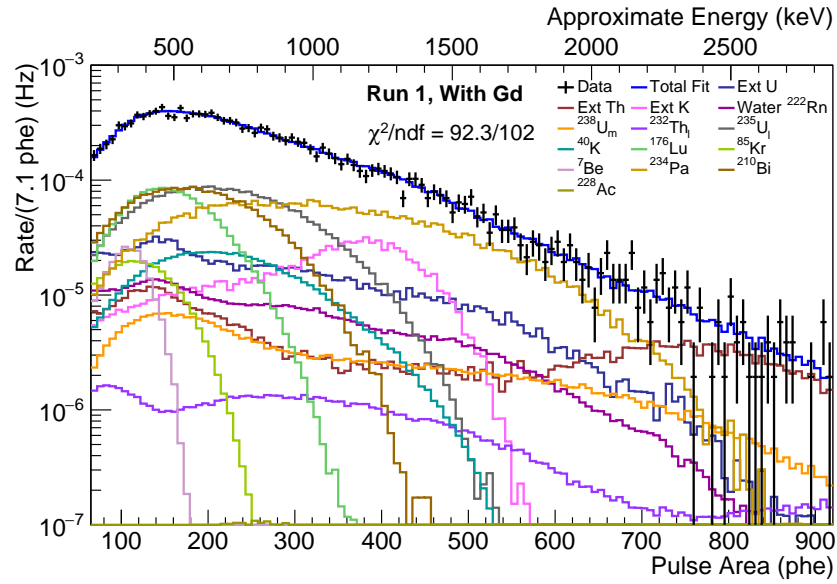


(a)

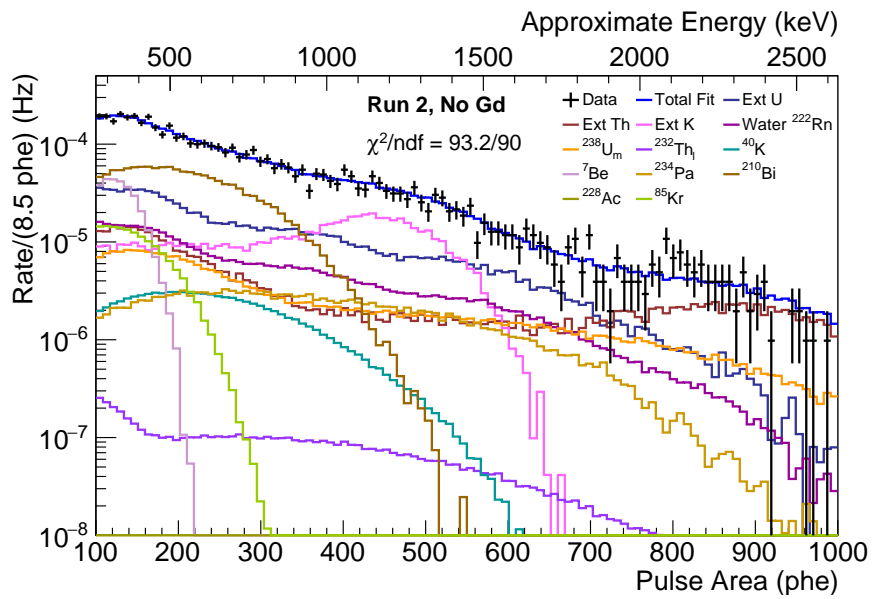


(b)

Figure 16: Best-fit to selection of  $\alpha$  events in (a) the GdLS sample and (b) the unloaded LS sample. A full color version of this image is available online.



(a)



(b)

Figure 17: Best-fit to selection of  $\gamma/\beta$  events in (a) the GdLS sample and (b) the unloaded LS sample. A full color version of this image is available online.

### 7.6. Inclusive Fits and Results

The inclusive Screener count rates above 200 keV implied by the radioimpurity concentrations of the previous section are within  $1.7\sigma$  of that observed in data. An additional inclusive fit was performed in each run to observe how the above results change under the constraint of equal rates, with no selection on pulse shape imposed. During the fit, all isotope populations begin with the concentrations measured in Tab. 7 and are constrained by those errors as well. For each of the  $^{238}\text{U}_m$ ,  $^{235}\text{U}_1$ , and  $^{232}\text{Th}_1$  subchains, the  $\alpha$  and  $\beta$  emitting isotopes are summed into single populations. Furthermore, to reduce the number of fit parameters, the  $^{238}\text{U}_m$  and  $^{232}\text{Th}_1$  populations are fixed, as their rates are subdominant and have already been measured by counting pulse pairs in Sec. 7.2. The  $^{235}\text{U}_1$  population is allowed to float as the combined rate from its  $\alpha$  activity forms a very prominent feature in the pulse area spectrum of Run 1.

The inclusive fit results are given in Tab. 9 where the results of the previous section are also repeated for comparison. The fits and their residuals are shown in Fig. 18 and Fig. 19. Generally, we find a uniform reduction in concentration across all the isotope populations. We note, however, the  $2.6\sigma$  discrepancy between results for  $^{176}\text{Lu}$  in Run 1. Two attempts were made to rectify these results. First, the  $^{176}\text{Lu}$  rate was fixed, which resulted in a change of  $\Delta\chi^2 = 9.0$ . Second, the constraint on  $^{210}\text{Bi}$  was removed as its shape is similar to that of  $^{176}\text{Lu}$ . In this iteration the best fit  $^{176}\text{Lu}$  and  $^{210}\text{Bi}$  rates were the same as that reported here.

Table 9: Radioimpurity concentrations measured in the  $\alpha$  &  $\beta/\gamma$  fits and using the inclusive fit in both loaded and unloaded LS runs grouped by isotope type. Reported errors are statistical only and, where none are given, the one-sided upper limit at 90% CL is reported. A 0.4% systematic error resulting from the uncertainty on the LS mass in the detector also applies.

	Isotope	Gd-Loaded LS Activity (mBq/kg)		Unloaded LS Activity (mBq/kg)	
		$\alpha$ & $\gamma/\beta$ Fit	Inclusive Fit	$\alpha$ & $\gamma/\beta$ Fit	Inclusive Fit
$^{238}\text{U}$ Chain	$^{238}\text{U}, ^{234}\text{U}$	$0.23 \pm 0.02$	$0.20 \pm 0.01$	-	-
	$^{238}\text{U}, ^{234}\text{U}, ^{230}\text{Th}$	-	-	$0.0055 \pm 0.0052$	$< 1.3$
	$^{234}\text{Pa}$	$0.33 \pm 0.04$	$0.31 \pm 0.02$	$< 0.065$	$0.021 \pm 0.007$
	$^{238}\text{U}_m$ Subchain	$0.019 \pm 0.003$		$0.023 \pm 0.002$	
	$^{210}\text{Bi}$	$0.40 \pm 0.26$	$0.39 \pm 0.12$	$0.30 \pm 0.10$	$0.19 \pm 0.01$
	$^{210}\text{Po}$	$0.16 \pm 0.02$	$0.11 \pm 0.02$	$0.099 \pm 0.009$	$0.08 \pm 0.01$
$^{235}\text{U}$ Chain	$^{235}\text{U}_1$ Subchain	$0.185 \pm 0.006$	$0.19 \pm 0.02$	-	-
$^{232}\text{Th}$ Chain	$^{232}\text{Th}$	$0.16 \pm 0.04$	$0.10 \pm 0.02$	$0.059 \pm 0.013$	$0.037 \pm 0.008$
	$^{228}\text{Ac}$	$< 0.20$	$< 0.08$	$< 0.018$	$< 0.010$
	$^{232}\text{Th}_1$ Subchain	$0.0071 \pm 0.0019$		$0.00082 \pm 0.00074$	
Other	$^{40}\text{K}$	$< 0.34$	$0.20 \pm 0.08$	$< 0.14$	$0.015 \pm 0.008$
	$^7\text{Be}$	$< 2.69$	$< 2.93$	$1.67 \pm 0.51$	$1.16 \pm 0.59$
	$^{85}\text{Kr}$	$< 0.31$	$< 0.29$	$0.069 \pm 0.067$	$< 0.02$
	$^{176}\text{Lu}$	$0.25 \pm 0.07$	$0.08 \pm 0.06$	-	-

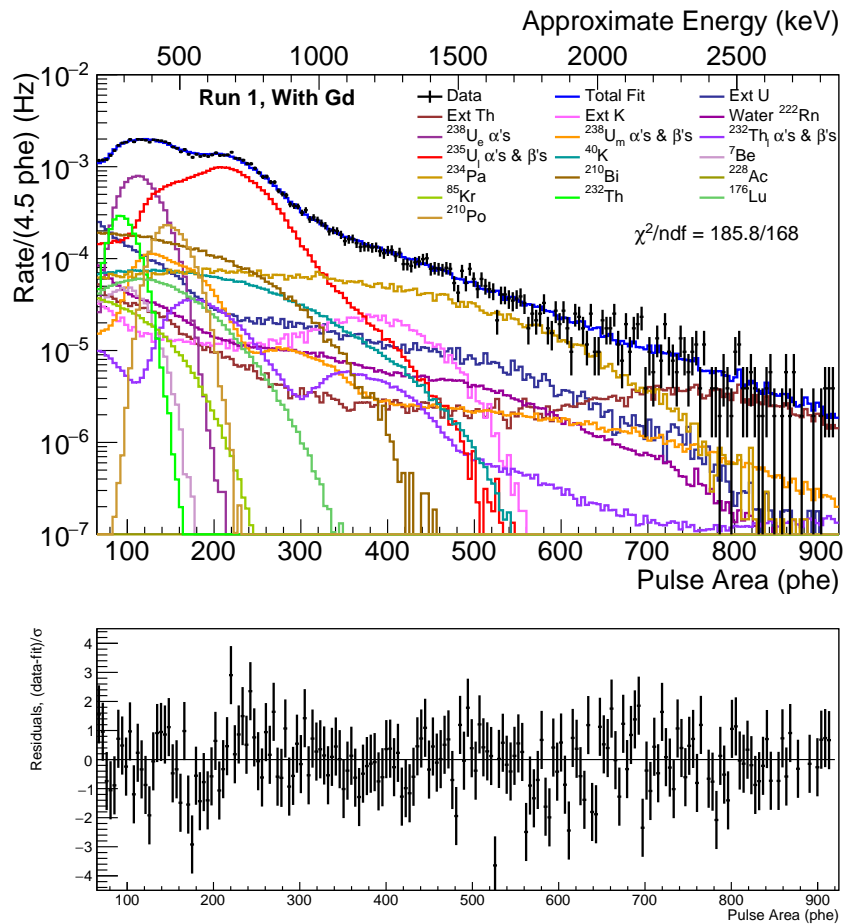


Figure 18: Inclusive fit to Run 1 data and fit residuals. A full color version of this image is available online.



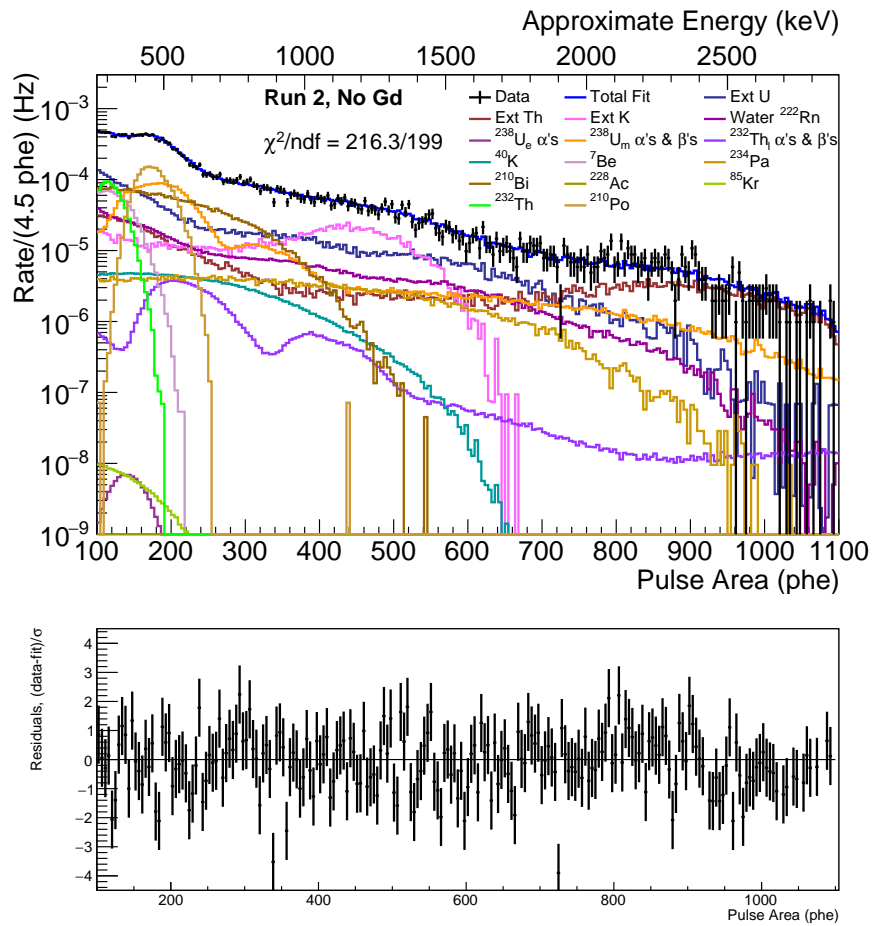


Figure 19: Inclusive fit to Run 2 data and fit residuals. A full color version of this image is available online.

### 7.7. Rates in the OD

In Tab. 10 we use the Screener results from Tab. 7 to predict the contributions to the singles rate in the 17.3 tonnes of LS in the LZ OD. Rates are reported separately for  $\alpha$  and  $\beta/\gamma$  decays and also given assuming no energy threshold and a 100 keV threshold. The contribution from  ${}^7\text{Be}$  is not included as its half-life is small compared to the planned length of the experiment [9]. Similar results for the total  $\alpha$  and  $\beta/\gamma$  rates in the OD derived from the inclusive fits given Tab. 9 are consistent within the errors given here.

Table 10: Predictions for the singles rate in 17.3 tonnes of LS in the OD calculated from the values in Tab. 7. Rates are given in the case of no energy threshold and a 100 keV threshold for both the unloaded and Gd-loaded LS.

Source	Decay Type	Gd-Loaded LS Rate (Hz)		Unloaded LS Rate (Hz)	
		No Threshold	>100 keV	No Threshold	>100 keV
${}^{238}\text{U}$ Chain	$\alpha$	$12.4 \pm 0.6$	$12.4 \pm 0.6$	$3.6 \pm 0.2$	$3.6 \pm 0.2$
	$\beta/\gamma$	$22.5 \pm 6.4$	$11.9 \pm 4.0$	$11.4 \pm 2.5$	$5.4 \pm 1.5$
	All	$34.8 \pm 6.4$	$24.3 \pm 4.0$	$15.0 \pm 2.5$	$9.0 \pm 1.5$
${}^{235}\text{U}$ Chain	$\alpha$	$19.2 \pm 0.3$	$19.2 \pm 0.3$	0	0
	$\beta/\gamma$	$9.6 \pm 0.2$	$5.8 \pm 0.1$	0	0
	All	$28.8 \pm 0.3$	$25.0 \pm 0.3$	0	0
${}^{232}\text{Th}$ Chain	$\alpha$	$3.4 \pm 0.7$	$3.4 \pm 0.7$	$1.1 \pm 0.2$	$1.1 \pm 0.2$
	$\beta/\gamma$	$0.2 \pm 3.9$	$0.2 \pm 2.7$	$0.0 \pm 0.3$	$0.0 \pm 0.2$
	All	$3.6 \pm 4.0$	$3.6 \pm 2.8$	$1.1 \pm 0.4$	$1.1 \pm 0.3$
${}^{40}\text{K}$	$\beta/\gamma$	$1.7 \pm 3.1$	$1.6 \pm 2.9$	$0.3 \pm 1.7$	$0.3 \pm 1.6$
${}^{85}\text{Kr}$	$\beta/\gamma$	$1.9 \pm 2.8$	$1.5 \pm 2.2$	$1.2 \pm 1.2$	$0.9 \pm 0.9$
${}^{176}\text{Lu}$	$\beta/\gamma$	$4.3 \pm 1.2$	$4.3 \pm 1.2$	0	0
${}^{14}\text{C}$	$\beta$	$82.5 \pm 1.7$	$7.0 \pm 0.2$	$82.5 \pm 1.7$	$7.0 \pm 0.2$
${}^{152}\text{Gd}$	$\alpha$	$27.9 \pm 1.4$	$17.0 \pm 0.9$	0	0
${}^{147}\text{Sm}$	$\alpha$	$18.2 \pm 1.8$	$13.5 \pm 1.4$	0	0
<b>Total</b>	$\alpha$	$81.1 \pm 2.5$	$65.5 \pm 1.9$	$4.7 \pm 0.3$	$4.7 \pm 0.3$
<b>Total</b>	$\beta/\gamma$	$122.8 \pm 8.8$	$32.5 \pm 6.1$	$95.4 \pm 3.7$	$13.7 \pm 2.4$
<b>Total</b>	All	$203.9 \pm 9.2$	$97.9 \pm 6.4$	$100.1 \pm 3.7$	$18.3 \pm 2.4$

In the OD,  $n$ 's which moderate and subsequently capture in the GdLS can be tagged by the unique combination of a prompt, quenched proton recoil signal followed by a delayed electron recoil signal from the cascade of  $n$ -capture  $\gamma$ 's. In the cases where the proton recoil signal is below threshold or non-existent, internal  $\beta/\gamma$  decays can mimic the delayed  $n$ -capture signature. Internal  $\alpha$ -decays, however, can be identified as being  $\alpha$ -like by their pulse shape and so contribute less to the overall false veto probability. Use of a 200 keV threshold in the OD additionally reduces the rate from radioimpurities to  $(56.8 \pm 5.5)$  Hz primarily by excluding pulses from  ${}^{14}\text{C}$ ,  ${}^{152}\text{Gd}$ , and  ${}^{147}\text{Sm}$ .

The overall cleanliness of the OD will be higher than that achieved in runs with the Screener. In particular, we expect the rate from  ${}^{210}\text{Pb}$  daughters to be reduced through minimized exposure of OD components with radon-laden air. This includes not only the acrylic tanks themselves but also the inside surfaces of the LS filling system. Further improved filling techniques will also minimize the concentration of  ${}^{85}\text{Kr}$  and  ${}^{222}\text{Rn}$  in the final GdLS. With these considerations the GdLS mixture measured here should be suitable for use in the LZ OD.

## 8. Conclusion

Efficient tagging of background  $n$ 's in LZ will be accomplished with the use of an OD containing an LS mixture loaded with Gd at 0.1 % by mass. The LZ requirement for a false veto rate  $<5$  % imposes a limit on the concentration of radioimpurities that can contribute to the OD singles rate above a 100 keV threshold. The average impurity level should be  $\lesssim 0.07$  mBq/kg.

A small acrylic detector was constructed and operated in the extremely low-background environment of the former LUX water tank to assess the radiopurity of the GdLS. The use of radiopure materials and the very low-background R11410-20 PMTs allows for  $\approx 10^{-4}$  mBq/kg sensitivity to radioimpurities in the LS. The detector was used to count samples of both Gd-loaded and unloaded LS. A higher activity from internal radioimpurities is detected in the loaded LS, in agreement with the general experience of experiments seeking to detect neutrinos and antineutrinos.

PSD was used to separately select events from  $\alpha$ 's and those from  $\gamma/\beta$ 's. The fits to the resulting pulse area spectra provide a measurement of the concentrations of various radioisotopes in the LS samples. In particular, the detector is sensitive to the rate of  $\alpha$ -decays throughout the  $^{238}\text{U}$ ,  $^{235}\text{U}$ , and  $^{232}\text{Th}$  decay chains. Our results demonstrate that secular equilibrium is broken in all three chains. In the GdLS, the dominant activity is found to be from the  $^{231}\text{Pa}$  or  $^{227}\text{Ac}$  subchain of the  $^{235}\text{U}$  series. The strong  $\gamma$ -line from  $^{235}\text{U}$  at the head of this decay chain was not detected in a HPGe screening of the purified Gd additives used in the loading process. The HPGe assay results generally agree within errors with those obtained in the Screener. The discrepancy in the measured  $^{232}\text{Th}_e$  concentrations is possibly explained by removal of  $^{228}\text{Ra}$  during the Gd additive purification.

The  $^{14}\text{C}/^{12}\text{C}$  ratio of the unloaded LS was measured to be  $(2.83 \pm 0.06(\text{stat.}) \pm 0.01(\text{sys.})) \times 10^{-17}$ , the sensitivity of our detector being comparable to that of detectors two orders of magnitude more massive.

The expected rate in the LZ OD from GdLS radioimpurities derived using the Screener measurements is  $97.9 \pm 6.4$  Hz above a 100 keV threshold. The majority of this rate results from  $\alpha$ -decays in the scintillator. An increase in threshold to 200 keV will remove pulses from low-energy decays such as those from  $^{14}\text{C}$ ,  $^{152}\text{Gd}$ , and  $^{147}\text{Sm}$  and results in a predicted rate of  $(56.8 \pm 5.5)$  Hz which is suitably low for use in the LZ OD. It was noted that delayed signals from  $\alpha$  events will contribute less to the overall false veto probability of the OD through the use of PSD techniques. Improved cleanliness procedures and more aggressive purification of the Gd compound will also help to lower the rate further.

## 9. Acknowledgments

The authors would like to acknowledge contributions to this work from the following groups within the LZ collaboration: Brown University for providing the R11410-20 PMTs, University of California-Davis for providing amplifiers, and University of Rochester for providing the SkuTek DDC-10 digitizer. We also wish to acknowledge S.A. Hertel for use of the thoron source and V.A. Kudryavtsev for estimates of the expected  $^7\text{Be}$  concentration.

This work was supported by the U.S. Department of Energy (DOE) under award

numbers DE-SC0011702, DE-AC02-05CH11231, and DE-SC0012704.

We acknowledge many types of support provided to us by the South Dakota Science and Technology Authority (SDSTA), which developed the Sanford Underground Research Facility (SURF) with an important philanthropic donation from T. Denny Sanford as well as support from the State of South Dakota. SURF is operated by the SDSTA under contract to the Fermi National Accelerator Laboratory for the DOE, Office of Science.

## References

### References

- [1] R. D. Albert, An anticoincidence gamma-ray scintillation spectrometer, *Rev. Sci. Instrum.* 24 (12) (1953) 1096–1101. doi:10.1063/1.1770609.
- [2] S. Landsberger, S. Peshev, Compton suppression neutron activation analysis: Past, present and future, *J. of Radioanal. Nucl. Ch.* 202 (1) (1996) 201–224. doi:10.1007/BF02037943.
- [3] F. S. Goulding, D. A. Landis, P. N. Luke, N. W. Madden, D. F. Malone, R. H. Pehl, A. R. Smith, Semiconductor detectors and double beta decay, *IEEE Trans. on Nucl. Sci.* 31 (1) (1984) 285–299. doi:10.1109/TNS.1984.4333263.
- [4] K. S. Hirata, et al., Observation in the Kamiokande-II Detector of the Neutrino Burst from Supernova SN 1987a, *Phys. Rev. D* 38 (1988) 448–458. doi:10.1103/PhysRevD.38.448.
- [5] Y. Fukuda, et al., The Super-Kamiokande detector, *Nucl. Instrum. Meth. A* 501 (2003) 418–462. doi:10.1016/S0168-9002(03)00425-X.
- [6] D. Yu. Akimov, et al., The ZEPLIN-III Anti-Coincidence Veto Detector, *Astropart. Phys.* 34 (2010) 151–163. arXiv:1004.4207, doi:10.1016/j.astropartphys.2010.06.010.
- [7] C. Ghag, et al., Performance of the veto detector incorporated into the ZEPLIN-III experiment, *Astropart. Phys.* 35 (2011) 76–86. arXiv:1103.0393, doi:10.1016/j.astropartphys.2011.06.006.
- [8] B. J. Mount, et al., LUX-ZEPLIN (LZ) Technical Design Report arXiv:1703.09144.
- [9] D. S. Akerib, et al., Projected WIMP Sensitivity of the LUX-ZEPLIN (LZ) Dark Matter Experiment arXiv:1802.06039.
- [10] J. Heise, The Sanford Underground Research Facility at Homestake, *J. Phys. Conf. Ser.* 606 (1) (2015) 012015. arXiv:1503.01112, doi:10.1088/1742-6596/606/1/012015.
- [11] M. Agostini, et al., First Simultaneous Precision Spectroscopy of  $pp$ ,  ${}^7\text{Be}$ , and  $pep$  Solar Neutrinos with Borexino Phase-II (2017). arXiv:1707.09279.
- [12] A. Gando, et al.,  ${}^7\text{Be}$  Solar Neutrino Measurement with KamLAND, *Phys. Rev. C* 92 (5) (2015) 055808. arXiv:1405.6190, doi:10.1103/PhysRevC.92.055808.
- [13] A. G. Piepke, S. W. Moser, V. M. Novikov, Development of a Gd loaded liquid scintillator for electron anti-neutrino spectroscopy, *Nucl. Instrum. Meth. A* 432 (1999) 392–398. arXiv:nucl-ex/9904002, doi:10.1016/S0168-9002(99)00530-6.

- [14] F. Boehm, et al., Final results from the Palo Verde neutrino oscillation experiment, *Phys. Rev. D* 64 (2001) 112001. [arXiv:hep-ex/0107009](#), doi:10.1103/PhysRevD.64.112001.
- [15] F. P. An, et al., Measurement of electron antineutrino oscillation based on 1230 days of operation of the Daya Bay experiment, *Phys. Rev. D* 95 (7) (2017) 072006. [arXiv:1610.04802](#), doi:10.1103/PhysRevD.95.072006.
- [16] J. H. Choi, et al., Observation of Energy and Baseline Dependent Reactor Antineutrino Disappearance in the RENO Experiment, *Phys. Rev. Lett.* 116 (21) (2016) 211801. [arXiv:1511.05849](#), doi:10.1103/PhysRevLett.116.211801.
- [17] Y. Abe, et al., Improved measurements of the neutrino mixing angle  $\theta_{13}$  with the Double Chooz detector, *JHEP* 10 (2014) 086, [Erratum: *JHEP*02,074(2015)]. [arXiv:1406.7763](#), doi:10.1007/JHEP02(2015)074, 10.1007/JHEP10(2014)086.
- [18] P. Fernández, Status of GADZOOKS!: Neutron Tagging in Super-Kamiokande, *Nucl. Part. Phys. Proc.* 273-275 (2016) 353–360. doi:10.1016/j.nuclphysbps.2015.09.050.
- [19] J. P. Pérez, Radioactive Contamination in Neutrino Experimental Physics: the Cases of NEXT and Super-Kamiokande Experiments, Ph.D. thesis, Universidad Autonoma de Madrid (2017).
- [20] E. K. Hyde, I. Perlman, G. T. Seaborg, *The Nuclear Properties of the Heavy Elements Volume II: Detailed Radioactivity Properties*, Prentice-Hall, Inc., Englewood Cliffs, NJ, USA, 1964.
- [21] D. S. Akerib, et al., An Ultra-Low Background PMT for Liquid Xenon Detectors, *Nucl. Instrum. Meth. A* 703 (2013) 1–6. [arXiv:1205.2272](#), doi:10.1016/j.nima.2012.11.020.
- [22] D. S. Akerib, et al., The Large Underground Xenon (LUX) Experiment, *Nucl. Instrum. Meth. A* 704 (2013) 111–126. [arXiv:1211.3788](#), doi:10.1016/j.nima.2012.11.135.
- [23] F. An, et al., Neutrino Physics with JUNO, *J. Phys. G* 43 (3) (2016) 030401. [arXiv:1507.05613](#), doi:10.1088/0954-3899/43/3/030401.
- [24] P. Agnes, et al., The veto system of the DarkSide-50 experiment, *JINST* 11 (03) (2016) P03016. [arXiv:1512.07896](#), doi:10.1088/1748-0221/11/03/P03016.
- [25] R. S. Boiko, Chemical purification of lanthanides for low-background experiments, *Int. J. Mod. Phys. A* 32 (30) (2017) 1743005. doi:10.1142/S0217751X17430059.

- [26] M. E. Monzani, Characterization and calibration of the BOREXINO detector for Solar and Supernova Neutrinos, Ph.D. thesis, Diderot U., Paris (2005).  
URL [http://borex.lngs.infn.it/Thesis/M.E.Monzani\\_PhD\\_Thesis.pdf](http://borex.lngs.infn.it/Thesis/M.E.Monzani_PhD_Thesis.pdf)
- [27] G. J. Keefer, First observation of  ${}^7\text{Be}$  solar neutrinos with KamLAND, Ph.D. thesis, University of Alabama (September 2016).
- [28] D. C. Malling, S. Fiorucci, M. Pangilinan, J. J. Chapman, C. H. Faham, J. R. Verbus, R. J. Gaitskell, Dark Matter Search Backgrounds from Primordial Radionuclide Chain Disequilibrium, (unpublished) (2013). [arXiv:1305.5183](https://arxiv.org/abs/1305.5183).
- [29] B. J. Mount, et al., Black Hills State University Underground Campus, *Appl. Radiat. Isot.* 126 (2017) 130–133. doi:10.1016/j.apradiso.2017.02.025.
- [30] Reynolds Polymer Technology, Inc., 607 Hollingsworth Street, Grand Junction, CO 81505 (2018).
- [31] DowDupont Inc., 974 Centre Road, Wilmington, DE 19805 USA (2018).
- [32] Material Concepts, 11620 Caroline Road, Philadelphia, PA 19154-2116 (2018).
- [33] M. Janecek, W. W. Moses, Optical reflectance measurements for commonly used reflectors, *IEEE Trans. Nucl. Sci.* 55 (4) (2008) 2432–2437. doi:10.1109/TNS.2008.2001408.
- [34] M. Janecek, Reflectivity spectra for commonly used reflectors, *IEEE Trans. Nucl. Sci.* 59 (3) (2012) 490–497. doi:10.1109/TNS.2012.2183385.
- [35] Z.-Y. Yu, et al., Study of a prototype water Cherenkov detector for the Daya Bay neutrino experiment, *Nucl. Instrum. Meth. A* 682 (2012) 26–30. doi:10.1016/j.nima.2012.04.050.
- [36] E. Aprile, et al., Lowering the radioactivity of the photomultiplier tubes for the XENON1T dark matter experiment, *Eur. Phys. J. C* 75 (11) (2015) 546. [arXiv:1503.07698](https://arxiv.org/abs/1503.07698), doi:10.1140/epjc/s10052-015-3657-5.
- [37] D. S. Akerib, et al., Identification of Radiopure Titanium for the LZ Dark Matter Experiment and Future Rare Event Searches, *Astropart. Phys.* 96 (2017) 1–10. [arXiv:1702.02646](https://arxiv.org/abs/1702.02646), doi:10.1016/j.astropartphys.2017.09.002.
- [38] S. Agostinelli, et al., GEANT4: A Simulation toolkit, *Nucl. Instrum. Meth. A* 506 (2003) 250–303. doi:10.1016/S0168-9002(03)01368-8.
- [39] D. S. Akerib, et al., Measurement of the gamma ray background in the davis cavern at the sanford underground research facility Manuscript in preparation.
- [40] SkuTek Instrumentation, 150 Lucius Gordon Drive, Ste. 209, West Henrietta, NY 14586 - 9687, USA (2018).

- [41] National Fire Protection Association, Technical Correlating Committee on Flammable and Combustible Liquids, NFPA 30: Flammable and Combustible Liquids Code, National Fire Protection Association, 2018.
- [42] Y. Ding, J. Liu, Z. Wang, Z. Zhang, P. Zhou, Y. Zhao, A new gadolinium-loaded liquid scintillator for reactor neutrino detection, *Nucl. Instrum. Meth. A* 584 (2008) 238–243. doi:10.1016/j.nima.2007.09.044.
- [43] CEPSA Química Bécancour, Inc., 5250 Bécancour Boulevard, Bécancour (Québec) G9H 3X3 Canada (2018).
- [44] G. Alimonti, et al., Measurement of the  $^{14}\text{C}$  abundance in a low-background liquid scintillator, *Phys. Lett. B* 422 (1998) 349–358. doi:10.1016/S0370-2693(97)01565-7.
- [45] M. Yeh, J. B. Cumming, S. Hans, R. L. Hahn, Purification of lanthanides for large neutrino detectors: Thorium removal from gadolinium chloride, *Nucl. Instrum. Meth. A* 618 (2010) 124–130. doi:10.1016/j.nima.2010.02.124.
- [46] M. Furst, H. Kallmann, Energy transfer by means of collision in liquid organic solutions under high energy and ultraviolet excitations, *Phys. Rev.* 94 (1954) 503–507. doi:10.1103/PhysRev.94.503.
- [47] H.-L. Xiao, J.-S. Deng, N.-Y. Wang, Oxygen quenching in a lab based liquid scintillator and the nitrogen bubbling model, *Chin. Phys. C* 34 (5) (2010) 571–574. doi:10.1088/1674-1137/34/5/011.
- [48] H. Kallmann, M. Furst, Fluorescence of solutions bombarded with high energy radiation (energy transport in liquids) part ii, *Phys. Rev.* 81 (1951) 853–864. doi:10.1103/PhysRev.81.853.
- [49] W. Beriguete, et al., Production of a gadolinium-loaded liquid scintillator for the Daya Bay reactor neutrino experiment, *Nucl. Instrum. Meth. A* 763 (2014) 82–88. arXiv:1402.6694, doi:10.1016/j.nima.2014.05.119.
- [50] G. T. Wright, Absolute Quantum Efficiency of Photofluorescence of Anthracene Crystals, *Proc. of the Phys. Soc. B* 68 (4) (1955) 241–248. doi:10.1088/0370-1301/68/4/306.
- [51] G. T. Wright, Absolute Scintillation Efficiency of Anthracene Crystals, *Proc. of the Phys. Soc. B* 68 (11) (1955) 929–937. doi:10.1088/0370-1301/68/11/317.
- [52] C. N. Chou, The nature of the saturation effect of fluorescent scintillators, *Phys. Rev.* 87 (1952) 904–905. doi:10.1103/PhysRev.87.904.
- [53] J. B. Birks, Scintillations from Organic Crystals: Specific Fluorescence and Relative Response to Different Radiations, *Proc. of the Phys. Soc. A* 64 (10) (1951) 874–877. doi:10.1088/0370-1298/64/10/303.



- [54] C. J. Taylor, W. K. Jentschke, M. E. Remley, F. S. Eby, P. G. Kruger, Response of some scintillation crystals to charged particles, *Phys. Rev.* 84 (1951) 1034–1043. doi:10.1103/PhysRev.84.1034.
- [55] J. Heise, The Sanford Underground Research Facility, in: 15th International Conference on Topics in Astroparticle and Underground Physics (TAUP 2017) Sudbury, Ontario, Canada, July 24-28, 2017, 2017. arXiv:1710.11584. URL <https://inspirehep.net/record/1633645/files/arXiv:1710.11584.pdf>
- [56] B. R. Littlejohn, Observation of Antineutrino Disappearance at the Daya Bay Experiment, Ph.D. thesis, Wisconsin U., Madison (2012).
- [57] B. von Krosigk, Measurement of proton and  $\alpha$  particle quenching in LAB based scintillators and determination of spectral sensitivities to supernova neutrinos in the SNO+ detector, Ph.D. thesis, Technische Universität Dresden (June 2015).
- [58] H. M. O’Keeffe, E. O’Sullivan, M. C. Chen, Scintillation decay time and pulse shape discrimination in oxygenated and deoxygenated solutions of linear alkylbenzene for the SNO+ experiment, *Nucl. Instrum. Meth. A* 640 (2011) 119–122. arXiv:1102.0797, doi:10.1016/j.nima.2011.03.027.
- [59] H. Behrens, J. Janecke, Numerical Tables for Beta Decay, Vol. 4, Springer-Verlag, Berlin, 1969, in Landolt-Brnstein - Group I Elementary Particles, Nuclei and Atoms.
- [60] I. R. Barabanov, et al., Measurement of the  $^{14}\text{C}$  content in liquid scintillators by means of a small-volume detector in the low-background chamber of the baksan neutrino observatory, *Physics of Atomic Nuclei* 80 (6) (2017) 1146–1152, [*Yad. Fiz.* 80,no. 6, 665 (2017)]. doi:10.1134/S1063778817060059.
- [61] L. Baudis, A. Behrens, A. Ferella, A. Kish, T. Marrodan Undagoitia, D. Mayani, M. Schumann, Performance of the Hamamatsu R11410 Photomultiplier Tube in cryogenic Xenon Environments, *JINST* 8 (2013) P04026. arXiv:1303.0226, doi:10.1088/1748-0221/8/04/P04026.
- [62] XIA LLC, 31057 Genstar Rd, Hayward, CA 94544 (2018).
- [63] R. B. Vogelaar, J. Benziger, F. P. Calaprice, N. Darnton, Removal of cosmogenic  $^7\text{Be}$  from scintillators, *Nucl. Instrum. Meth.* 372 (1) (1996) 59 – 62. doi:10.1016/0168-9002(95)01239-7.
- [64] J. J. Back, Y. A. Ramachers, ACTIVIA: Calculation of Isotope Production Cross-sections and Yields, *Nucl. Instrum. Meth. A* 586 (2008) 286–294, (ACTIVIA). arXiv:0709.3472, doi:10.1016/j.nima.2007.12.008.
- [65] R. Ford, M. Chen, O. Chkvorets, D. Hallman, E. Vazquez-Jauregui, SNO+ scintillator purification and assay, *AIP Conf. Proc.* 1338 (2011) 183–194. doi:10.1063/1.3579580.

- [66] G. Keefer, et al., Laboratory studies on the removal of radon-born lead from KamLAND's organic liquid scintillator, *Nucl. Instrum. Meth. A* 769 (2015) 79–87. [arXiv:1312.0977](https://arxiv.org/abs/1312.0977), [doi:10.1016/j.nima.2014.09.050](https://doi.org/10.1016/j.nima.2014.09.050).